Spin Architectures for Investigating Quantum Phenomena: NMR and NV Centers in Diamond

A thesis

Submitted in partial fulfillment of the requirements of the degree of

Doctor of Philosophy

by:

V.S. Anjusha

Registration ID 20122037

Department of Physics

INDIAN INSTITUTE OF SCIENCE EDUCATION AND RESEARCH

PUNE-411008, India

Certificate

Certified that the work incorporated in the thesis entitled **"Spin Architectures for Investigating Quantum Phenomena: NMR and NV Centers in Diamond"** submitted by **V S Anjusha** was carried out by the candidate, under my supervision. The work presented here or any part of it has not been included in any other thesis submitted previously for the award of any degree or diploma from any other university or institution.

Date: (Supervisor)

Declaration

I declare that this written submission represents my ideas in my own words and where others ideas have been included, I have adequately cited and referenced the original sources. I also declare that I have adhered to all principles of academic honesty and integrity and have not misrepresented or fabricated or falsified any idea/data/fact/source in my submission. I understand that violation of the above will be cause for disciplinary action by the Institute and can also evoke penal action from the sources which have thus not been properly cited or from whom proper permission has not been taken when needed.

Date: (V.S. Anjusha)

Abstract

Quantum computer is known as the ”holy grail of science”. Many groups and companies are making great efforts to build a quantum computer. Quantum simulation is one of the key applications of a quantum computer. As the name suggests, quantum simulation is about simulating a quantum system which is less accessible and controllable using another quantum system which is more accessible and controllable. Spin architectures such as NMR and NV centers in diamond form a convenient testbed for the experimental investigations of quantum phenomena as well as quantum information. Realizing any arbitrary unitary is a major requirement of a quantum simulator. In this direction, the thesis focuses on quantum simulations and quantum controls using spin based quantum architectures.

The thesis is divided into two parts.The first part of the thesis discusses the experiments done on a NMR quantum simulator. We provided the first experimental investigation of the Quantum Pigeonhole effect using a four qubit NMR quantum register and the experimental details are discussed in Chapter 2. In this experiment, we adapted GRadient Ascent Pulse Engineering (GRAPE) technique for realizing unitary operators.

Later on, we realized unitary and non-unitary quantum controls by adapting bang-bang (BB) method. Using the pulses realized by bang-bang control, we implemented the Optimal Fixed-Point Quantum Search Algorithm on a three qubit NMR quantum register (Chapter 3). We also demonstrated realizing some nonunitary operations using BB along with Pulsed Field Gradients (PFG).

In Chapter 4 , we briefly discuss on realizing dynamically protected quantum gates by integrating Dynamical Decoupling (DD) and optimal control techniques. We experimentally showed protecting quantum discord during Grover’s search algorithm by applying protected quantum gates.

Then we come to the second part of the thesis which focuses on the experiments

done on nitrgen vacancy (NV) centers in nitrogen. We introduce the physical properties such as electronic energy levels and Hamiltonian of the NV centers in Chapter 5. In Chapter 6, we discuss the confocal setup and the microwave electronics for addressing and manipulating the electronic spin in NV center. Finally, We show some of the basic experiments performed on NV center based spin architecture.

To my **Family**

List of publications

1. **V. S. Anjusha**, S. S. Hegde and T. S. Mahesh, *NMR investigation of the quantum pigeonhole effect*, Phys. Lett, A **380 (4), 577-580 (2016)**.

2. G. Bhole, **V. S. Anjusha** and T. S. Mahesh, *Steering quantum dynamics via bang-bang control: Implementing optimal fixed-point quantum search algorithm*, Phys. Rev. A **93 (4), 042339 (2016)**.

3. **V. S. Anjusha** and T. S. Mahesh, *Optimized dynamical protection of nonclassical correlation in a quantum algorithm*, ArXiv preprint **ArXiv:1802.02792 (2018)**.

4. S. Pal, S. Moitra, **V. S. Anjusha**, A. Kumar, T. S. Mahesh, *Hybrid scheme for factorization: Factoring 551 using a 3-qubit NMR quantum adiabatic processor*, Pramana - J Phys **92: 26(2019)**.

5. V. R. Krithika, **V. S. Anjusha** and T. S. Mahesh, *NMR studies of quantum chaos in a two-qubit kicked top*, ArXiv preprint **arXiv:1810.11963 (2018)**.

Acknowledgments

I am grateful to many people for helping and supporting me to complete the first stage of my scientific career, the PhD. I am using this time to remember and thank to some of them who made it a special experience.

First and foremost, I would like to thank my supervisor, Dr T S Mahesh, for his constant guidance and support throughout my PhD. His enthusiasm and excitement for science are infectious and it made it easy for me to get constantly excited and motivated to work on my projects. His deep knowledge in the field is very inspiring. His humor and his spontaneity in coming up with new scientific ideas made our group meetings very joyful at the same time very helpful for me to learn new things.

I would like to extend my acknowledgment to my research advisory committee (RAC) members, Dr. Umakant Rapol and Dr. Rejish Nath. Their valuable feedbacks and suggestions during yearly RAC meetings greatly helped me to make progress in my projects thereby my thesis.

I also would like to thank all my collaborators, Prof. Anil Kumar, Swathi S Hegde, Gaurav Bhole, Rupak Bhattacharya, Soham, Koti kamineni Koteshwara Rao, Tanmoy Chakrobarthy and Phani Kumar. It was indeed a wonderful experience to work with them and I could learn many new things in the field of experimental quantum information. Rupak and I built the first NV setup in Dr. Mahesh's lab and he taught me everything about doing optics experiments right from the start like aligning the optics, handling optics etc. Apart from science, I always admired his deep knowledge in Indian classical music and I always enjoyed our discussions on music during tea breaks from experiments.

I am very grateful to all my labmates, Abhishek Shukla, Swathi S Hegde, Sudheer Kumar, Deepak Khurana, Soham Pal, Krithika, Gaurav, Rupak and Priya for all those useful discussions we used to have and those discussions made many difficult concepts easier for me to understand and comprehend.

It is never enough to thank my batchmates Tomin, Chetan, Meghna , Abhishek, Aditi Nandi, Sneha, hridya and Prachi for being a constant source of entertainment. Especially, I am very indebted to Chetan for helping me at any time by going out of his way. The discussions we used to have on anything under the sun at the night canteen were refreshing after a long day at lab.

I would like to thank my besties in IISER, Hridya, Krithika, Dibyatha, Prachi, Ajith ,Giri and Sumit for making my life outside lab more colorful and filled with beautiful moments. All the fun activities, 'mad tea parties' at my room and traveling we did together will be deeply missed. Thank you, Hridya for being my "partner in crime" and I will miss our evening walk and our cooking experiments when the mess food becomes a nightmare.I was very lucky to get a Junior cum best friend like Krithika and working on a project together was a pleasant memory. I would like to thank Ajith and Dibyata for being the great critiques of me and every time it helped me to become a better person. I always enjoyed science discussions with Sumit whom we fondly called "bro". He was very caring like a brother. Our dinner is never fulfilling without Prachi's very un-realistic dreams and stories which we often refer as "Prachi logic". Although Giri spent very little time with us together as he had to move to London, he has been always an integral part of our friends circle ever since we met. I am very sure that our friendship will continue as strong as before even after my PhD.

It was a great opportunity for me to spend the last year of my PhD at Prof. Fedor Jelezko's lab at University of Ulm. His deep knowledge and experience in applications of nitrogen vacancy (NV) centers in diamond greatly helped me to write the second part of my thesis. Discussions with Jochen and Christoph helped me to understand NV center experiments better and it helped me to improved the second part of my thesis.

Last but not least, I am thankful to my family, Achan, Amma, Sruthy (Aparna) and brother in law for their all supports and encouragements throughout my PhD. My family is incomplete without my grandparents and they have been always the most delightful people in my life. I am very lucky to have cool grandparents like them. And, Special thanks to my beautiful little Niece, Nithara; it was the desire to meet her soon propelled me to write this thesis faster.

Contents

List of Figures

List of Tables

Chapter 1

Introduction

Quantum Information Processing

Quantum information processing (QIP) [25, 75] is an interdisciplinary field of research that combines areas like theoretical and experimental physics, mathematics, computer science, material science and engineering. QIP is the way of information processing and computation by taking advantage of quantum mechanical laws such as superposition of the quantum states and entanglement. Simulating a quantum system on a classical computer becomes impossible when the system size gets bigger as it requires huge memory to store the state of the system [20]. 1n 1982, Richard Feynman put forward the idea of simulating a quantum system using another quantum system which is more accessible and controllable. He said ”let the quantum computer itself be built with quantum mechanical elements which obey quantum mechanical laws” [33]. Apart form simulating quantum systems, in 1984 C. Bennett and G. Brassard presented cryptographic key distribution model using Weisner’s conjugate coding on a quantum computer [7]. This work opened up a secured way for communication and cryptography. In 1991, A. Eckart proposed protocol for secure quantum communication based on quantum entanglement [28, 48]. The first quantum algorithm was developed by Peter shor at Bell laboratory for the prime factorization of a large number in the year of 1994 [87, 88]. This work was in-fact a major challenge for many of the existing encryption codes such as RSA code. The codes like RSA exploit the difficulty of prime factorization on a classical computer. Followed by Shor's algorithm, in 1996, Lov Grover again from Bell laboratory came up with an algorithm for data search on a unsorted data base. This algorithm offers a quadratic speed up over any of the existing classical search algorithm [40, 41]. In the same year, Lyod showed that a quantum computer can indeed act like a universal quantum simulator [59]. That means, a quantum computer can be initialized and be measured after performing universal set of quantum gates.The first experimental quantum information processing was demonstrated by David Cory et al. and Neil Gershenfeld and Isaac Chuang on the same year of 1997 using liquid state NMR. In this chapter, I shall discuss the basics introduction for QIP [21, 38].

Quantum bit

A quantum bit or qubit is considered as the basic unit of quantum information processing analogous to a bit in classical computer. However, if a bit can take either 1 or 0 as an input, the quantum superposition allows a qubit to exist in both possible sates simultaneously. The two possible states of the qubit is generally represented by $|0\rangle$ and $|1\rangle$. And,the state of a qubit can be written as,

$$\psi = \alpha|0\rangle + \beta|1\rangle \tag{1.1}$$

where, $\alpha^2 + \beta^2 = 1$. The probability amplitudes α and β are in general complex numbers.The matrix representation of the above state can be written as $\psi = \begin{bmatrix} \alpha \\ \beta \end{bmatrix}$. A measurement made on the state gives the outcome either $|0\rangle$ with a probabilty $|\alpha|^2$ or $|1\rangle$ with a probability $|\beta|^2$. Often, the state of a qubit is represented a vector on a Bloch sphere of unit radius as shown in Fig.1.1. Now, the equ.1.1 can be rewritten as,

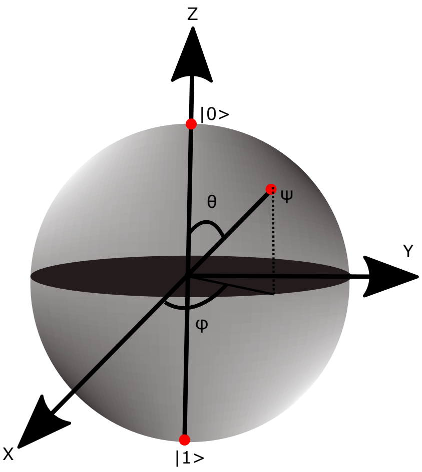

Figure 1.1: Bloch sphere representation of a qubit

$$\psi = \cos(\theta)|0\rangle + e^{i\phi}\sin(\theta)\beta|1\rangle \tag{1.2}$$

where, θ and ϕ are the polar and azimuthal angles respectively.

Now consider a quantum register of n qubits and the state of the quatum register can be expressed as the tensor product of individual states. And,it can be written as,

$$\psi = \sum_{1}^{n} \psi_1 \otimes \psi_2 \cdots \psi_n \tag{1.3}$$

for example,for a 2 qubit quantum register the state can be written as,

$$\psi = \alpha_1|0\rangle + \beta_1|1\rangle \otimes \alpha_2|0\rangle + \beta_2|1\rangle = \alpha_1\alpha_2|00\rangle + \alpha_1\beta_2|01\rangle + \beta_1\alpha_1|10\rangle + \beta_1\beta_2|11\rangle \tag{1.4}$$

where,

$$|00\rangle = \begin{bmatrix}1\\0\end{bmatrix} \otimes \begin{bmatrix}1\\0\end{bmatrix} = \begin{bmatrix}1\\0\\0\\0\end{bmatrix}; \quad |01\rangle = \begin{bmatrix}1\\0\end{bmatrix} \otimes \begin{bmatrix}0\\1\end{bmatrix} = \begin{bmatrix}0\\0\\1\\0\end{bmatrix};$$

$$|10\rangle = \begin{bmatrix}0\\1\end{bmatrix} \otimes \begin{bmatrix}1\\0\end{bmatrix} = \begin{bmatrix}0\\1\\0\\0\end{bmatrix}; \quad 101\rangle = \begin{bmatrix}0\\1\end{bmatrix} \otimes \begin{bmatrix}0\\1\end{bmatrix} = \begin{bmatrix}0\\0\\0\\1\end{bmatrix};$$

Density Matrix

The another way of expressing the sate of a quantum register is using a vector in a Liouville space and it is called a density matrix. This is often required when we deal with a statical ensemble of quantum system as in Nuclear Magnetic Resonance (NMR) QIP. Assume we have ensemble of states ψ_i with probabilities p_i, then the density matrix of the total system can be expressed as,

$$\rho = \sum_i p_i |\psi_i\rangle\langle\psi_i| \tag{1.5}$$

where, $\sum p_i = 1$.

When $\mathrm{Tr}\rho^2 = 1$, then system is in a pure state that means all members of the ensemble are in the same state. The condition for system being in a mixed state is, $\mathrm{Tr}\rho^2 < 1$. A density matrix must satisfy the following three conditions:

- ρ is Hermitian. i.e.,$\rho = \rho^\dagger$
- ρ is a positive operator such that all eigenvalues are nonnegative.
- $\mathrm{Tr}[\rho] = 1$

The most general density matrix representation for asingle qubit is,

$$\rho = \frac{\mathbb{I} + \vec{r}.\vec{\sigma}}{2} \tag{1.6}$$

where, $\mathbb{I}$ is the identity matrix, $\vec{r}$ is the 3D Bloch vector and $\vec{\sigma} = \sigma_x\vec{x} + \sigma_y\vec{y} + \sigma_z\vec{z}$ is the Pauli vector operator. And,

Quantum Entanglement

Quantum entanglement is one of the unique quantum mechanical phenomena. And, it is an important resource for quantum communication, quantum computation and cryptography. Consider a composite system with n components. Then, the system is in a entangled state if the total state of the composite system can not be expressed as a tensor product of states of the each component. ie,

$$\psi \neq \psi_1 \otimes \psi_2 \cdots \psi_n \tag{1.7}$$

and this is called the non-separability criterion for an entangled state.

the most famous examples for a maximally entangled states are the Bell states and these states are expressed as;

$$\phi_{\pm} = \frac{|00\rangle \pm |11\rangle}{\sqrt{2}} \tag{1.8}$$

and

$$\psi_{\pm} = \frac{|01\rangle \pm |10\rangle}{\sqrt{2}} \tag{1.9}$$

Here, the measurement made on one of the qubits affect the measurement outcome of the other qubit. for example in the state $\phi_{\pm}$, the measurement made on the first qubit gives the output either $|0\rangle$ or $|1\rangle$ with $50:50$ probabilities. If the measurement outcome of the first qubit is $|0\rangle$ then simultaneously the second qubit also collapses to the qubit state $|0\rangle$.

Quantum Gates

Analogous to classical computers, the qubit manipulations are done by performing some local as well as nonlocal quantum operators and those are called quantum gates. Unlike classical gates, quantum gates are unitary operators which satisfy the condition $UU^{\dagger} = \mathbb{I}$. Consequently, all operations performed on a quantum register are reversible. In this section, I will describe some of the basic quantum gates.

Single Qubit Gates

NOT Gate: This gate is very similar to the NOT operation in classical information. This gate acted upon a qubit transforms the state $|0\rangle$ to $|1\rangle$ and vice- versa. This operator is nothing but the Pauli operator σ_x and the matrix form of this operator can be written as;

$$X = \begin{bmatrix} 0 & 1 \\ 1 & 0 \end{bmatrix}.$$

Hadamard Gate: Hadamard (H) gate acted upon the state $|0\rangle$ transforms this into a equal superposition state $|+\rangle = \frac{|0\rangle+|1\rangle}{\sqrt{2}}$ and $|1\rangle$ into the state $|-\rangle = \frac{|0\rangle-|1\rangle}{\sqrt{2}}$. The matrix form of H is;

$$H = \frac{1}{\sqrt{2}} \begin{bmatrix} 1 & 1 \\ 1 & -1 \end{bmatrix}.$$

Phase Gate: The Phase gate (R_ϕ) operated on the basis state $|1\rangle$ take it to $e^{i\phi}|1\rangle$ and leaves the basis state $|0\rangle$ unchanged as $Z|0\rangle = |0\rangle$. And,the matrix form of Z gate is;

$$R_\phi = \begin{bmatrix} 1 & 0 \\ 0 & e^{i\phi} \end{bmatrix}.$$

where,ϕ is the phase sift.

Non-local Quantum Gates

Non-local quantum operators are applied on more than one qubits simultaneously. Controlled-NOT (CNOT) gate is one of the examples for a Non-local quantum gates.

CNOT: CNOT gate is often used for selectively inverting a target qubit. The target qubit flips when the controlled qubit is in the state $|1\rangle$ else it remain unchanged. The matrix representation of this operator is;

$$CNOT = \begin{bmatrix} 1 & 0 & 0 & 0 \\ 0 & 1 & 0 & 0 \\ 0 & 0 & 0 & 1 \\ 0 & 0 & 1 & 0 \end{bmatrix}.$$

Quantum Measurements

Quantum measurement is one of the most intricate problems in quantum mechanics. There are various measurements schemes in quantum mechanics and Projective measurement is the most basic measurement scheme. Apart form projective measurements, other schemes like weak measurements and Positive Operator Valued Measurements (POVM) are also getting more popular in QIP.

Projective Measurements: Quantum measurements are described by a set of measurement operator M_m which form a complete basis such that $\sum M_m = \mathbb{I}$. The state of the quantum system can be written as;

$$\psi = \sum_m C_m|m\rangle \tag{1.10}$$

The post measurement state is given by;

$$\psi_m = \frac{M_m|\psi\rangle}{P_m} \tag{1.11}$$

where, $P_m = \langle\psi|M_m M_M^\dagger|\psi\rangle$ is the probabilities of measurement outcomes.

POVM: POVM is considered as the most general scheme for quantum measurement as the measurement operators M_m not necessarily orthogonal. The POVM measurement elements are defined as; $E_m = M_m M_m^\dagger$ with the condition $\sum_m E_m = \mathbb{I}$. The probability of the outcome is $P_m = \langle\psi|E_m|\psi\rangle$.

Ensemble Average: The measurement outcome of a quantum mechanical event is probabilistic. Therefore, the measurement has to be done on multiple copies of the state which is to be measured. Ensemble average is another way for obtaining the expectation value of an observable 'A'. In this case, large number of quantum systems are prepared in the same state with corresponding density matrix ρ, and the expectation value of A is given by;

$$\langle A\rangle = \mathrm{Tr}[\rho A] \tag{1.12}$$

Divincenzo's criteria

A Qubit can be realised using any two level quantum system. And such systems are abundant in nature. But, according to Divincenzo's criteria, not all quantum system can be used for QIP tasks. He proposed a list of minimal requirements for a physical implementation of a quantum computer. The criteria are the following;

- A scalable physical system with a well defined qubit.
- Ability to initialize system to any quantum state.
- Long relevant decoherence time.
- A Universal set of quantum gates.
- Qubit specific measurement.

There are two more additional criteria which are mostly relevant for quantum communication tasks. The remaining two criteria are:

- The ability to inter convert stationary and flying qubits .
- The ability to faithfully transmit flying qubits between specified locations.

Experimental Architectures

Various physical systems have been anticipated for building a quantum computer based on Divincenzo's criteria. However, none of them satisfies all 7 criteria. And it is still a question which one of them is going be the full fledged quantum computer. And, these are some of the architectures:

- Nuclear Magnetic Resonance (NMR).
- Nitrogen Vacancy (NV) Center .

- Superconducting Quantum Interference Device (SQUID).
- Trapped Atom/Ion.
- Linear Optics
- Quantum Dots.

This thesis covers both NMR and NV center architectures. In the following section, we will discuss the basics of NMR. And, NV centers will be discussed in the second part of the thesis.

Nuclear Magnetic Resonance

Many Nuclei posses an intrinsic physical property called Spin. It can be either an intiger or a integer multiplication of 1/2. All spins have magnetic moment and a spin acts like a tiny magnet. In NMR QIP, a qubit is realized using a spin 1/2 nucleus in an external magnetic field, B_0. When a spin 1/2 nucleus is placed in a magnetic field, it's energy eigenstates will split under Zeeman Hamiltonian (see Fig.1.2). The energy required to induce flipping and obtain an NMR signal is the energy difference between these levels, $\Delta E = \gamma h B_0/2\pi$ where γ is the gyro-magnetic ratio of the nucleus and $h = 6.63 \times 10^{-27}$ erg sec is the Planck's constant. The energy gap ΔE is in RF range. From the Bohr condition, $\Delta E = h\nu$, the frequency of the nuclear transition can be written as;

$$\nu_0 = \gamma B_0/2\pi \qquad (1.13)$$

This is called the Larmor resonance frequency. This is often in rf range and the system is irradiated with an RF radiation. When the frequency of the RF matches with the ν_0, the resonance occurs. This phenomenon is popularly known as the nuclear magnetic resonance (NMR).

Figures/nmr_Zeeman.pdf

Many qubits can be realized if the NMR system has more than one NMR active nuclei. In that scenario, there will be additional interactions other than Zeeman interaction. In this section, we will discuss all possible interactions in NMR Hamiltonian [56].

Zeeman interaction

Let us consider a particle with spin, I and the corresponding angular momentum, $\mu = \gamma h\mathbf{I}/2\pi$ where, γ is the gyromagnetic ratio of the nucelus , h is the Planck's constant and **I** is the spin operator. Let us now apply a magnetic field,B_0 along the z axis and the corresponding Zeeman interaction Hamiltonian is given by;

$$H_{Zeeman} = -\gamma\hbar B_0 I_z \tag{1.14}$$

where, I_z is the z component of the Spin operator and $\hbar = h/2\pi$. A spin I nucleus has (2I+1) energy eigenstates under Zeeman Hamiltonian with eigenvalues, $E_m = -\gamma\hbar B_0 m$ where, $m = -I, -I+1 \cdots I-1, I$ and $E_{m+1} - E_m = \Delta E = \hbar\omega_0$ where $\omega_0 = -\gamma B_0$ is the Larmor frequency. In NMR QIP, the qubit is realized by the case I=1/2.

Chemical Shift

Now consider the case where we have two spin 1/2 particles of same species, i.e, both are having the same gyro-magnetic ratio. Nevertheless, the local magnetic field felt by the individual nuclei need not be the same. This is because the local field is the sum of external field and the induced field by the nearby diamagnetic electrons. The chemical environment is different for different nuclei, hence the local fields are different. Therefore, the local field can be written as,

$$B_{Loc} = B_0(1 - \sigma_0) \tag{1.15}$$

where, σ_0 is called the Chemical shift tensor. This often plays a major role in addressing different qubits in NMR.

J- Coupling

It is an indirect interaction between two nuclei due to the hyperfine interaction between the nuclei and the local electrons. This is also known as spin-spin or indirect dipole-dipole interaction. Two nuclear spins are indirectly connected via a magnetic interaction transmitted by the bonding electrons. In isotropic liquid state NMR, the Hamiltonian corresponding to this interaction is written as,

$$H_J = 2\pi \sum_{i<j}^{n} J_{ij} I^i \cdot I^j \tag{1.16}$$

where, J_{ij} is the J-coupling or the scalar coupling and I^i and I^j are the spin operator of the i^{th} and the j^{th} spin respectively.

Dipole-Dipole Interaction

A nucleus behaves like a tiny magnet and it possesses a magnetic dipole moment. Two nuclei interact with each other directly through space. This interaction is called direct dipole-dipole (DD) interaction. The Hamiltonian corresponding to DD interaction of twonuceli is given by;

$$H_{DD} = b^{ij} A + B + C + D + E + F \tag{1.17}$$

where,

$$\begin{aligned} A &= I_z^i I_z j 1 - 3\cos^2(\theta) \\ B &= \frac{-1}{4}(I_+^i I_-^j + I_-^i I_+^j)(1 - 3\cos^2(\theta) \\ C &= \frac{-3}{2}(I_+^i I_z^j + I_z^i I_+^j)(\sin(\theta)\cos(\theta)e^{i\phi}) \\ D &= \frac{-3}{2}(I_-^i I_z^j + I_z^i I_-^j)(\sin(\theta)\cos(\theta)e^{i\phi}) \\ E &= \frac{-3}{4}(I_+^i I_+^j)(\sin^2(\theta)e^{i2\phi}) \\ F &= \frac{-3}{4}(I_-^i I_-^j)(\sin^2(\theta)e^{i2\phi}) \end{aligned} \tag{1.18}$$

with polar coordinates θ and ϕ and r_{ij} is the vector connecting the i^th and j^th spin. The spin operators $I_+ = I_x + iI_y$ and $I_- = I_x - iI_y$ are called the ladder operators. And, $b^{ij} = -\mu_0\gamma^i\gamma^j\hbar/4\pi r_{ij}^3$ is the dipolar coupling constant, where $\mu_0 = 4\pi \times 10^-7N.A^{-2}$ is the magnetic permeability of free space and γ^n is the gyromagnetic ratio of the nuclear spin. Under secular approximation for the weekly coupled system or a heteronucelar system, the Hamiltonian become,

$$H_{DD} = 2d^{ij} I_z^i I_z^j \tag{1.19}$$

However, in liquid state NMR, due to the fast tumbling motion, this interaction gets averaged out to zero.

Qudrupolar Interaction

A nuclear spin with $I > 1/2$ possesses a quadrupolar charge distribution and consequently an associated electric quadrupolar moment. This qudrupole moment interacts with its surrounding electric filed gradient.For a nuclear spin oriented an angle θ with the external magnetic field which is assumed to be along the z axis, the first order quadrupole Hamiltonian can be written as,

$$H_Q = \frac{\omega_Q}{6}(3I_z^2 - I(I+1)) \tag{1.20}$$

with $\omega_Q = \frac{eQ\bar{V^{zz}}}{2I(2I-1)\hbar}$ where, e is the electronic charge, Q is the quadrupole moment and $\bar{V^{zz}}$ is the parallel component of the electric field tensor.

Quantum states in NMR

NMR is an ensemble quantum computer. Therefore, at thermal equilibrium the system is in a completely mixed state and the corresponding density matrix is given by,

$$\rho_{eq} = \frac{e^{-H_z/K_BT}}{Z} \tag{1.21}$$

where, H_z is the internal Hamiltonian with corresponding partition function Z, K_B is the Boltzmann constant and T is the absolute temperature [17]. This is a diagonal matrix with diagonal elements,

$$\rho_{eq} = \frac{e^{-E_i/K_BT}}{\sum_i^N e^{-E_i/K_BT}} \tag{1.22}$$

where E_i gives the population corresponding to different energy levels and N is the dimension of the Hilbert space. At higher temperature T, $E_i << K_BT$, then the ρ_{eq} can be approximated by,

$$\begin{aligned} \rho_{eq} &\approx (\mathbb{I} - H_z/K_BT)/\mathrm{Tr}(\mathbb{I} - H_z/K_BT) \\ &\approx \mathbb{I}/N - H_z/NK_BT \end{aligned} \tag{1.23}$$

The term $\mathbb{I}/N$ is unaffected by the unitary transformations hence it does not contribute to the NMR signal.Therefore this therm can be neglected during NMR experiments. Now consider an ensemble of M spin 1/2 nuclei. The corresponding thermal equilibrium

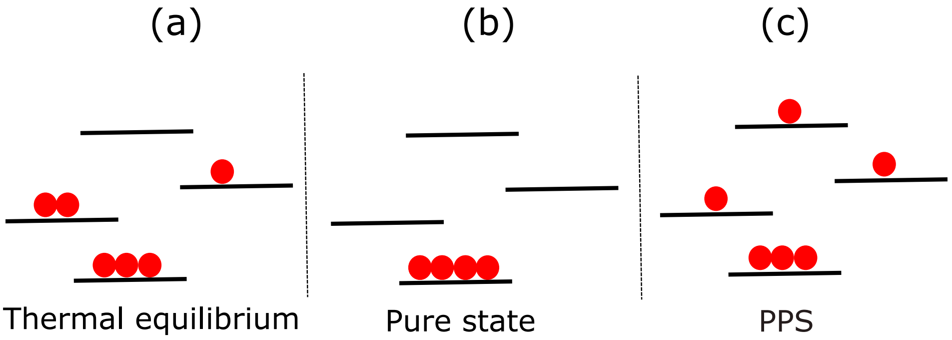

Figure 1.3: population distribution for a 2 qubit system, a) Thermal equilibrium state, b) Pure state, and c) PPS. Image taken and modified from [89].

density matrix in terms of Zeeman Hamiltonian can be written as,

$$\rho_{eq} = \sum_{k=1}^{M} \frac{\hbar\omega_{0k}}{NK_BT} I_{kz} \tag{1.24}$$

where, $\epsilon = \sum_{k=1}^{M} \frac{\hbar\omega_{0k}}{NK_BT}$ is generally called the purity factor and it is $\approx 10^{-5}$ for $M = 1$ at room temperature.

Pseudo Pure state: The system need to be initialized into a pure state for carrying out QIP tasks. That is all members in the ensemble has to be initialized into a single state $|\psi\rangle$ with corresponding density matrix, $\rho = |\psi\rangle\langle\psi|$. In practice, it is very difficult to achieve this condition. Nevertheless, this can be overcome by preparing the system into a Pseudo Pure state (PPS) state. The PPS density matrix can be written as,

$$\rho_{pps} = (1-\epsilon)\mathbb{I}/N + \epsilon\rho \tag{1.25}$$

In PPS, all states except one state have equal population. The population distribution in different NMR states are illustrated in Fig.1.3.

Spin manipulations using RF field

A system initialized into a density matrix, $\rho(0)$ evolve to a final density matrix $\rho(t)$ via a unitary transformation. And this can can be expressed as,

$$\rho(t) = U\rho(0)U^\dagger \tag{1.26}$$

where U is a unitary operator with a condition, $UU^\dagger = U^\dagger U = \mathbb{I}$.In quantum information language, these are called quantum gates. A single qubit quantum gates can be realized by a rotation about an axis $\hat{n}$ on a Bloch sphere and it is given by,

$$R_{\hat{n}}^{\theta} = e^{i\theta\hat{n}\cdot\sigma/2} = \cos(\theta/2)\mathbb{I} - i\sin\theta/2(\hat{n}_x\sigma_x + \hat{n}_y\sigma_y + \hat{n}_z\sigma_z) \tag{1.27}$$

where, $\hat{n} \in \hat{n_x}, \hat{n_y}, \hat{n_z}$ is the 3-D unit vector, $\sigma \in X, Y, Z$ are the Pauli matrices and θ is the angle of rotation. And nonlocal operators such as CNOT gates can be realized by the rotations along with free evolution operator under J-coupling.

In NMR, single qubit rotations are realized with the help of RF field applied perpendicular to the external magnetic field B_0. The RF Hamiltonian can be written as,

$$H_{rf} = -\gamma B_1(\cos(\omega_{rf}t + \phi)I_x + \sin(\omega_{rf}t + \phi)I_y) \tag{1.28}$$

where $\omega_1 = -\gamma B_1$ is the rf amplitude, ω_{rf} is the rf frequency and ϕ is the rf phase. The resonance condition is met when $\omega_{rf} = \omega_0$ where, ω_0 is the Larmor frequency of the spin. Let us first consider the resonance case with $\omega_{rf} = \omega_0$. Under rotating frame frame approximation, the effective rf Hamiltonian becomes,

$$H_{eff} = \omega_1(\cos(\phi)I_x + \sin(\phi)I_y) \tag{1.29}$$

Now suppose there is an offset, $\Omega = \omega_0 - \omega_{rf}$, the effective Hamiltonian will have an additional term along the longitudinal axis. Now, the effective Hamiltonian is written as,

$$H_{eff} = \Omega I_z + \omega_1(\cos(\phi)I_x + \sin(\phi)I_y) \tag{1.30}$$

This is equivalent to say, on resonance condition the effective field is along the $\hat{x}$ axis and it is on the $\hat{x} - \hat{z}$ plane when there is an offset. And, the nuclear spin will start nutating around the effective field with a nutation frequency, $\omega_{eff} = \sqrt{\Omega^2 + \omega_1^2}$. Therefore, any angle of rotation, θ can be realized by choosing the RF duration, τ such that $\omega_1\tau = \theta$.

NMR Readout

In NMR, the state readout is carried out with the aid of an RF coil placed along the sample. The measurement observable is the bulk transverse magnetization of the ensemble. At thermal equilibrium, the bulk magnetization vector points along the external field B_0 and a RF field, B_1, applied along the transverse plane, flips the magnetization to the transverse plane. Now, the bulk magnetization precesses around the transverse field and produces electromotive field in the coil placed around the sample tube in accordance of the Faraday's law of induction. However, due to decoherence and the static field inhomogeneity, the induced field will start decaying with time and it is called the free induction decay(FID). The NMR spectrum is obtained by Fourier transforming the FID signal.

The final bulk magnetization can be expresses as,

$$M(t) \propto \mathrm{Tr}(\rho(t)D_{op}) \tag{1.31}$$

where, $M(t) = M_x + iM_y$, $\rho(t)$ is the final density matrix and $D_{op} = I_x + iI_y$ is the detection operator. The signal in frequency domain is obtained via Fourier transformation of $M(t)$.

Chapter 2

NMR investigation of quantum pigeonhole effect

In this chapter, I will discuss the NMR simulation of a recent quantum phenomenon called quantum pigeonhole effect using unitary operators realized via GRadient Ascent Pulse Engineering (GRAPE) technique.

Introduction

Quantum theory has been often known for contradicting logics applied to our everyday life and quantum pigeonhole effect (QPHE) [1,2] is one of the examples. The pigeonhole principle is one of the most famous principles in mathematics and it states that if n items are put in $m < n$ containers, then at least one container must have more than one item [68]. Although, it is the simple logic for counting, it has got several interesting applications in mathematics [15,78,85], computer science [4,29,77], graph theory [100], and combinatorics [13].

Recently, Aharonov and coworkers have theoretically illustrated certain quantum mechanical scenarios appearing to contradict the pigeonhole principle [2]. This phenomenon, known as QPHE has already raised considerable interest. For example Yu

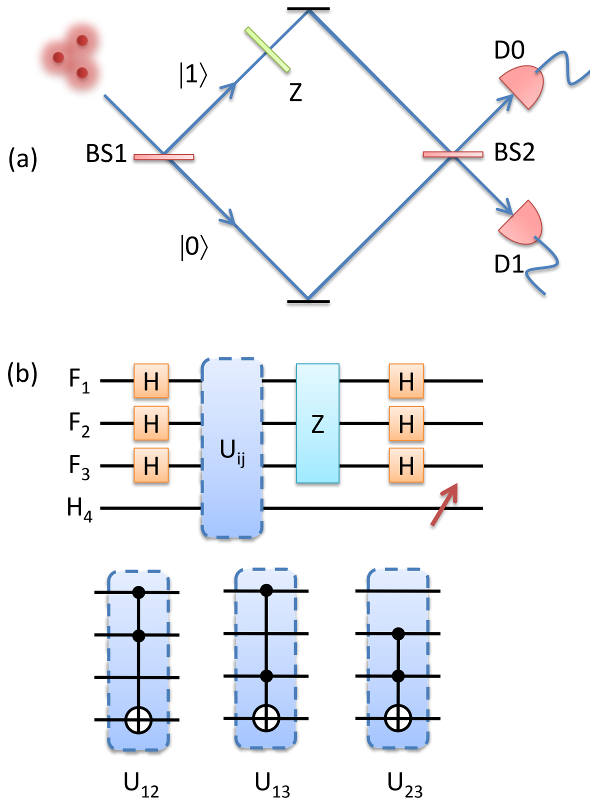

Figure 2.1: (a) Three quantum particles entering a Mach-Zehnder interferometer consisting of two beam-splitters (BS1 and BS2) and phase shifter (Z), and two particle-detectors D0 and D1. (b) Circuit for NMR investigation of QPHE. Hadamard gates perform the function of beam splitters, and Z-gate performs phase shift. Intermediate state information of the particle-qubits (F_1, F_2, F_3) is encoded onto an ancilla qubit (H_4) using one of the controlled operations U_{12}, U_{13}, and U_{23}. The ancilla qubit is measured at the end of the circuit.

and Oh demonstrated the emergence of QPHE from quantum contextuality [104]. Rae and Forgan suggested that QPHE arises as a result of interference between the wave-functions of weakly-interacting particles [81]. In this work, we simulate QPHE using a four-qubit NMR quantum simulator.

Theory

In the following section, I shall discuss the theoretical modeling of quantum pigeonhole effect(subsection 2.1). I will also briefly discuss the optimal control technique namely

GRAPE algorithm for realizing unitary operators for quantum simulation (subsection 2.2).

Quantum Pigeonhole Effect (QPHE)

Let us discuss the theory of QPHE by considering three identical particles simultaneously entering a Mach-Zender interferometer as shown in Fig. 2.1 (a). The Mach-zender interferometer consists of two beam-splitters (BS1 and BS2), a 90 degree phase-shifter (Z), and two identical detectors (D0 and D1). BS1 is used to create a superposition of two paths labelled $|0\rangle$ and $|1\rangle$. When a particle initially prepared in state $|0\rangle$ enters BS1, it transforms to $|+\rangle = (|0\rangle + |1\rangle)/\sqrt{2}$. Both paths are guided towards BS2 using mirrors. After the 90 degree phase-shifter Z, the state of the particle is $|+i\rangle = (|0\rangle + i|1\rangle)/\sqrt{2}$, and after BS2 it becomes $\{(1+i)|0\rangle + (1-i)|1\rangle\}/2$. Thus the particle has equal probability of reaching either of the detectors. The state $|+\rangle$ can also be written in terms of $|\pm i\rangle$, i.e.,

$$|+\rangle = \frac{1-i}{2}|+i\rangle + \frac{1+i}{2}|-i\rangle. \tag{2.1}$$

We notice that the first component, namely $|+i\rangle$ transforms to $|-\rangle = (|0\rangle - |1\rangle)/\sqrt{2}$ after Z, and then to $|1\rangle$ after BS2, and finally ends up in detector D1. Similarly, the second component, namely $|-i\rangle$ transforms to $|+\rangle = (|0\rangle + |1\rangle)/\sqrt{2}$ after Z, and then to $|0\rangle$ after BS2, and finally ends up in detector D0. In this sense, a measurement outcome of $|0\rangle$ (or $|1\rangle$) amounts to postselecting $|-i\rangle$ (or $|+i\rangle$) state just before the phase-shifter.

Suppose, three particles are initially in a state $|000\rangle$ and after BS1, the state of the particles is described by the superposition $|\psi_a\rangle = |+,+,+\rangle$. The final state may collapse with equal probability to any one of the states $\{|000\rangle, |001\rangle, |010\rangle, |011\rangle, |100\rangle,$ $|101\rangle, |110\rangle, |111\rangle\}$.

The projectors

$$P_{12} = |0\rangle\langle 0| \otimes |0\rangle\langle 0| \otimes \mathbb{1} + |1\rangle\langle 1| \otimes |1\rangle\langle 1| \otimes \mathbb{1} \tag{2.2}$$

$$P_{13} = |0\rangle\langle 0| \otimes \mathbb{1} \otimes |0\rangle\langle 0| + |1\rangle\langle 1| \otimes \mathbb{1} \otimes |1\rangle\langle 1| \tag{2.3}$$

$$P_{23} = \mathbb{1} \otimes |0\rangle\langle 0| \otimes |0\rangle\langle 0| + \mathbb{1} \otimes |1\rangle\langle 1| \otimes |1\rangle\langle 1|, \tag{2.4}$$

probe if any two of the particles are in the same state, i.e., $|00\rangle$ or $|11\rangle$. The expectation values of the projectors give corresponding probabilities. Evaluating the expectation values for the state $|+,+,+\rangle$, we find that $\langle P_{12}\rangle = \langle P_{23}\rangle = \langle P_{13}\rangle = 1/2$. Just after BS1, the probability for any two particles being in the same path is therefore $1/2$.

We shall now consider only the cases wherein all the three particles reach the same detector, say D0 (or D1) and discard all other possibilities. Then the measurement outcome $|000\rangle$ (or $|111\rangle$) is equivalent to postselecting the state $|\phi_1\rangle = |-i,-i,-i\rangle$ (or $|\phi_0\rangle = |+i,+i,+i\rangle$) before the phase-shifter.

The projection $|\psi^{same}_{j,k}\rangle = P_{jk}|\psi_a\rangle$ describes the component of $|\psi_a\rangle$ corresponding to particles j and k being in the same path. Since,

$$\langle\phi_0|\psi^{same}_{1,2}\rangle = \langle -i,-i,-i|P_{12}|+,+,+\rangle \tag{2.5}$$

$$= \frac{\langle -i,-i,-i|0,0,+\rangle + \langle -i,-i,-i|1,1,+\rangle}{2} \tag{2.6}$$

$$= 0, \tag{2.7}$$

This is equivalent to saying that the postselected state $|\phi_0\rangle$ has no component having particles 1 and 2 in the same path. Owing to the symmetry in the pre- ($|\psi_a\rangle$) and post- ($|\phi_0\rangle$) selected states, the above conclusion can be extended to any pair of particles. This effect is interpreted as - if all the three particles have to reach the same detector D0, then no two particles can take the same path inside the Mach-Zender interferometer. Of course, similar interpretation can also be given for the case in which all the three

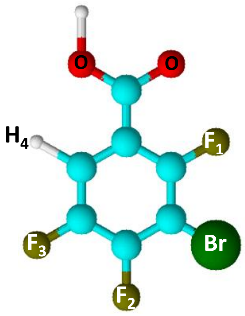

	F_1	F_2	F_3	H_4
F_1	7469	57	57	142
F_2		0	642	84.5
F_3			−9128	314
H_4				0

Figure 2.2: The molecular structure of 3-bromo-2,4,5-trifluorobenzoic acid. The chemical shifts (diagonal elements) and effective coupling constants J'_{ij} (off-diagonal elements) are shown in table. The NMR spectrum of ancilla is shown in Fig. 2.3(a).

particles reach the same detector D1. This phenomenon which seems to violate the classical pigeonhole effect is called QPHE.

GRAPE algorithm for realizing unitary operators

Realizing any arbitrary unitary is one of the major requirements for building a universal quantum simulator.Optimal control techniques have been extensively used for realizing robust quantum gates in NMR quantum simulator. In this work, we used GRAPE algorithm for realizing unitary operators required for the simulation.

GRAPE is a gradient based optimization algorithm. The goal of any optimization algorithm is to find the parameter co-ordinates (in n dimensional parameter space) where a cost function ϕ is either maximum or minimum. Calculating the gradient of the cost function at each point in the parameter space gives the direction to the maxima (see Fig.2.4).

Consider the total Hamiltonian of an NMR system which is of the form,

$$\mathcal{H}(t) = \mathcal{H}_{int} + \sum_{k=1}^{M} u_k(t) h_k \tag{2.8}$$

where, $\mathcal{H}_{int}$ is the internal Hamiltonian and the latter term is the rf Hamiltonian with rf

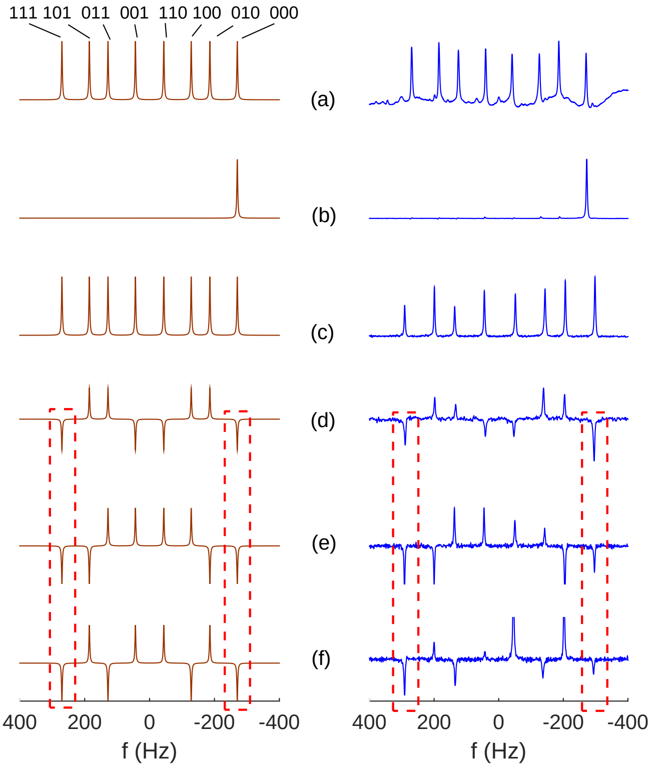

Figure 2.3: The ancilla NMR at various stages of QPHE simulation, each obtained by a final 90° detection pulse. The simulated and experimental spectra are shown in the left and right columns respectively. (a) Thermal equilibrium state ρ_{eq} (the background baseline is due to the liquid crystal signal), (b) The partial pseudopure state $\rho(0)$, and (c) after the entire MZI-circuit (without U_{ij}) indicating the various combinations of detections. Spectra in (d-f) correspond to the complete QPHE circuit shown in Fig. 2.1(b) obtained with U_{12}, U_{13}, and U_{23} respectively. The dashed boxes highlight the peaks corresponding to the postselected states as described in the text.

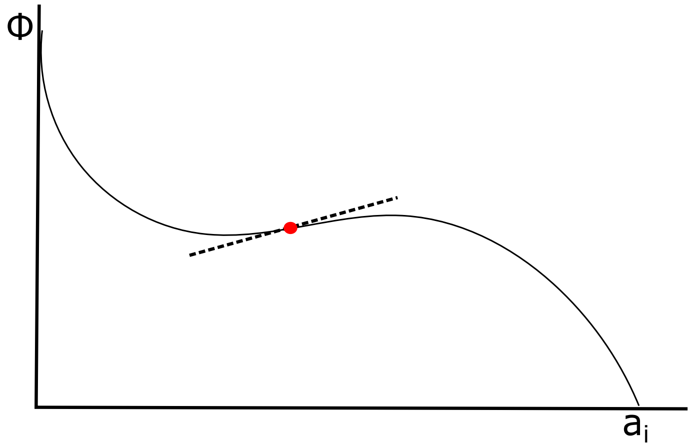

Figure 2.4: Gradient ascend algorithm

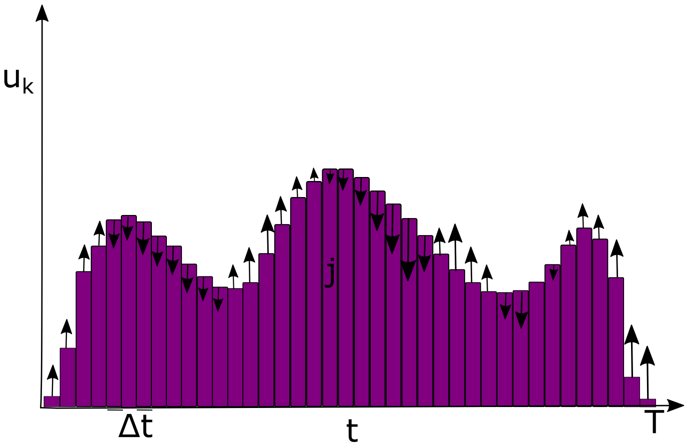

Figure 2.5: Schematic representation of the GRAPE algorithm. The control amplitude at each segment is assumed as a constant and the vertical arrows show the gradients indicating how each amplitude should be modified in the next iteration in order to improve the cost function.

amplitude, u_k, corresponding to different spin species, M and spin operator h_k. And, a total unitary operator at time, T can be written as,

$$U(T) = D\exp\left(-i\int_0^T \mathcal{H}(t)dt\right) \tag{2.9}$$

where, D is the Dyson time ordering operator coming from the time dependence of the Hamiltonian.

For the practical convenience, the total time, T, can be discretized into N step of $\Delta t = N/T$ duration and during each time step, the rf amplitude u_k can be treated as a constant as shown in Fig.2.5. Now the unitary corresponding to each segment j can be written as,

$$U_j = e^{-iH\Delta t} \tag{2.10}$$

and, the total unitary at time T is the cumulative product of the unitaries U_js. For a given Unitary U_{targ}, the goal is to optimize the rf amplitudes at each segment by maximizing a cost function which is nothing but the fidelity at time T in our case and is defined as,

$$\begin{aligned}\phi = \langle U_{targ} | U_T \rangle &= \langle U_{targ} | U_N ... U_1 \rangle && (2.11)\\ &= \langle U^\dagger_{j+1} ... U^\dagger_N \, U_{targ} | U_j ... U_1 \rangle && (2.12)\\ &= \langle P_j | X_j \rangle && (2.13)\end{aligned}$$

where, $P_j = U^\dagger_{j+1} ... U^\dagger_N \, U_{targ}$ is the backward evolving propagation starting form the target unitary, U_{targ}, and $X_j = U_j ... U_1$ is the forward evolving propagator at time $j\Delta t$.

The algorithm begins with initial guess amplitudes u_ks and in the next iteration, amplitudes get modified as

$$u_k(j) = u_k(j) + \epsilon \, \frac{\partial \phi_0}{\partial u_{k(j)}} \tag{2.14}$$

where, $\frac{\partial \phi_0}{\partial u_{k(j)}} = -\langle P_j | i \, \Delta t \, H_k \, X_j \rangle$ is the gradient at each segment j and ϵ is the step size (see Fig.2.2). The mathematics for getting the above expression for $\frac{\partial \phi_0}{\partial u_{k(j)}}$ can be found in reference [54]. We then repeat the algorithm until the desired fidelity has reached.

NMR simulation

We used a 4-qubit quantum register consists of 3-bromo-2,4,5-trifluorobenzoic acid (see Fig. 2.2) partially oriented in a liquid crystal N-(4-methoxybenzaldehyde)-4-butylanline (MBBA) for simulating QPHE. The three ^{19}F spins and the ^{1}H spin are respectively used as the three particle qubits and the ancilla qubit for encoding the intermediate path information. All the experiments were carried out on a 500 MHZ Bruker NMR spectrometer at an ambient temperature of 298 K. The effective couplings in this system are due to scalar interactions (J_{ij}) as well as partially averaged dipolar interactions (D_{ij}). Thus the internal Hamiltonian for the system, under weak-coupling approximation, can be written as

$$H = -2\pi \sum_i \nu_i I_{zi} + 2\pi \sum_{ij} J'_{ij} I_{zi} I_{zj}, \tag{2.15}$$

where ν_i are the resonance frequencies, $J'_{ij} = (J_{ij} + 2D_{ij})$ are the effective coupling constants, and I_{zi} is the z-component of spin angular momentum operator of ith spin [57]. All the relevant Hamiltonian parameters like chemical shifts and effective coupling constants are tabulated in Fig. 2.2.

The first step in the experiment is the initialization the particle-qubits (three ^{19}F nuclei) in a pseudo pure state and the ancilla can be still in thermal state. And, such state can be expressed as,

$$\rho(0) = \mathbb{1}/16 + \epsilon|000\rangle\langle 000| \otimes \sigma_z/2 \tag{2.16}$$

where $\epsilon \sim 10^{-5}$ is the purity factor. This state can be very easily realized by taking difference between two initial states: (i) ρ_{eq} corresponding to thermal equilibrium state and (ii) ρ_{in} obtained by inverting the populations of levels $|0000\rangle$ and $|0001\rangle$ using a low-power transition-selective Gaussian pulse of duration 80 ms [37]. The ancilla spectrum corresponding to the initial state obtained by a $90°$ detection pulse (shown in Fig. 2.3 (b)) clearly indicates the transition corresponding to the particle-state $|000\rangle$.

The next step is to apply the various elements of the Mach-Zehnder interferometer as shown in Fig. 2.1 (b). All the unitary operations were realized by GRAPE optimal control technique [53]. The durations of the GRAPE pulses ranged from 400 μs to 700 μs, and the fidelities were better than 0.99 over a 10 % RF inhomogeneity range.

The experimental spectrum after the complete MZI-circuit is shown in Fig. 2.3(c). To probe the component of the wave-function prior to the phase gate, we insert operator

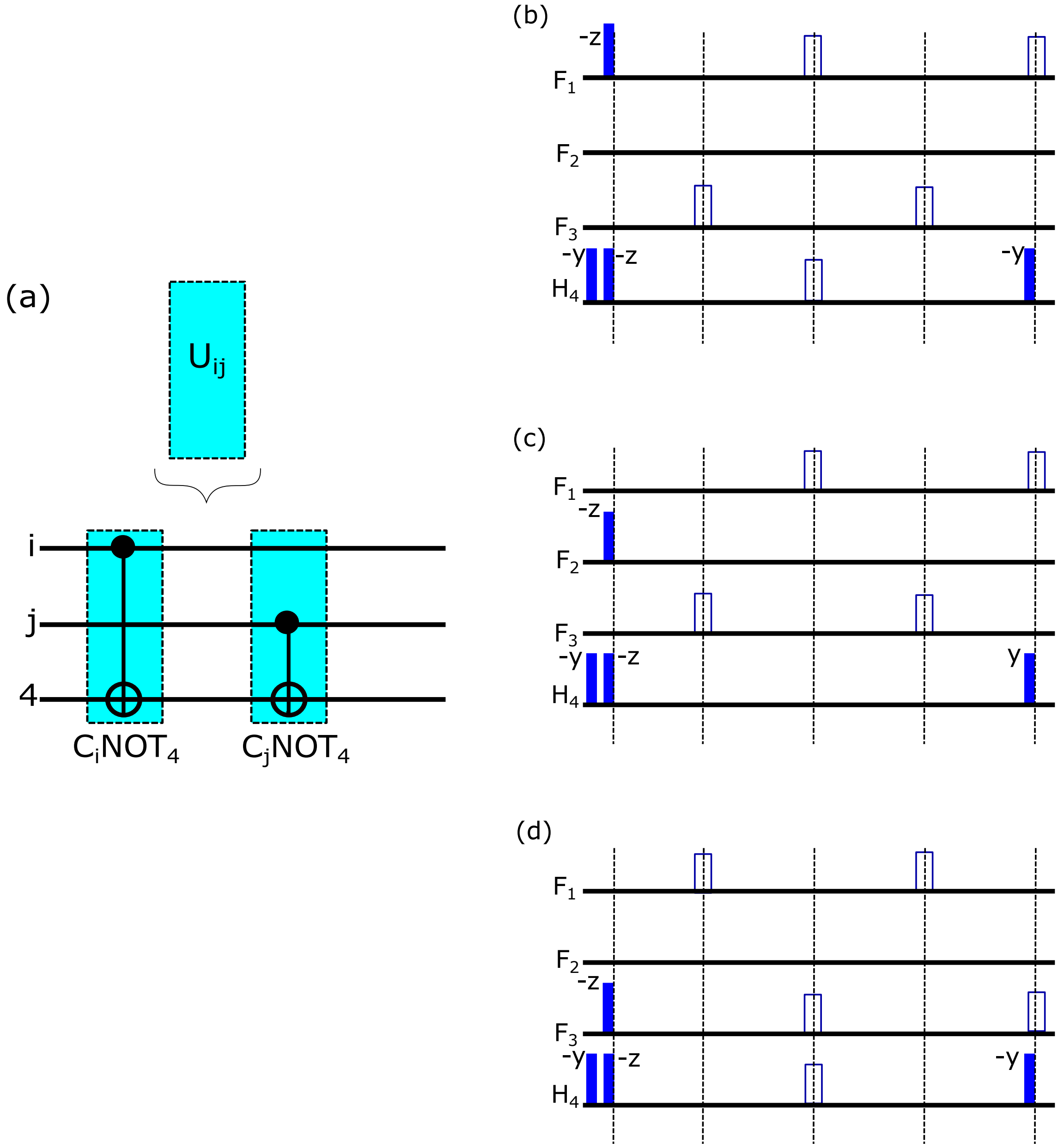

Figure 2.6: (a) Realizing U_{ij} by a pair of CNOT gates. (b-d) NMR pulse sequences corresponding to C_1NOT_4, C_2NOT_4, and C_3NOT_4 respectively. All the π pulses (open rectangles) are about y axis and the phases of the $\pi/2$ pulses (filled rectangles) are as indicated. The delays are set according to $\tau_i = 1/(8J'_{i,4})$.

U_{ij} as shown in Fig. 2.1 (b). The action of U_{ij} is given by

$$U_{ij} = P_{ij} \otimes \mathbb{1}_a + (\mathbb{1}_s - P_{ij}) \otimes X_a, \tag{2.17}$$

where P_{ij} are the projections as described in eqns. 2.4, $\mathbb{1}_s$, $\mathbb{1}_a$ are respectively the identity operators on system and ancilla, and X_a is the NOT operator on ancilla. Effectively, U_{ij} conserves the ancilla if particles i and j are in the same path, but inverts it otherwise. Thus in the ancilla NMR spectrum, a positive ancilla peak indicates two particles being in the same path, while a negative peak indicates them being in different paths. Each of the U_{ij} operations is realized by a pair of CNOT gates as described in Fig. 2.6 (a). The NMR pulse-sequences to generate each of the CNOT gates are shown in Fig. 2.6 (b-d).

The NMR spectra obtained after the complete MZI-circuit along with probing of particles $(1, 2)$ (by U_{12}), $(1, 3)$ (by U_{13}), and $(2, 3)$ (by U_{23}), are shown respectively on the right side of Figs. 2.3(d-f). The corresponding simulated spectra are shown on the left side. The intensity variations in the experimental spectra are mainly due to the imperfections in executing CNOT operations resulting from RF field inhomogeneities, nonlinearities of the RF amplifiers, as well as decoherence. However, we observe an overall agreement of the experimental results with the quantum theoretical simulations. In particular, we focus on the NMR transition 000 (111) corresponding to postselection of all the three particles reaching D0 (D1). These transitions are highlighted by dashed lines in Fig. 2.3(d-f)). All these transitions have negative intensities indicating that no two particles are in the same path. This is a clear demonstration of QPHE.

For three particles and two containers, the various other arrangements and their classical as well as quantum possibilities are shown in Table 1. Here the first two arrangements, where there is a clear contradiction between classical and quantum, correspond to QPHE. For the other cases, while the possibilities are probabilistic in the classical regime, they are certain in the quantum regime. Of course, it is also possible to gener-

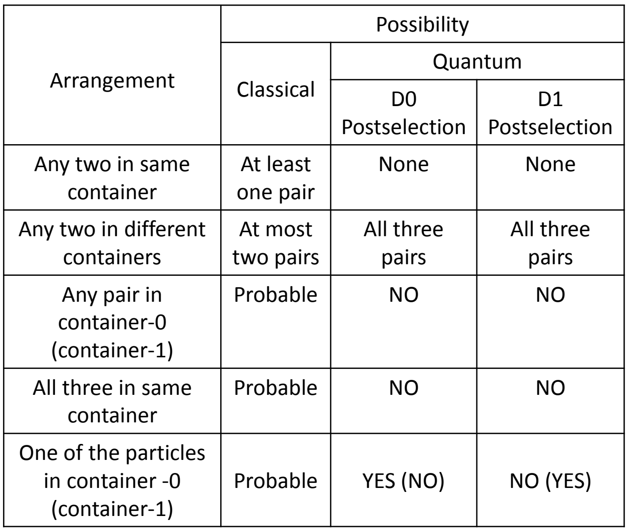

Arrangement	Possibility		
	Classical	Quantum	
		D0 Postselection	D1 Postselection
Any two in same container	At least one pair	None	None
Any two in different containers	At most two pairs	All three pairs	All three pairs
Any pair in container-0 (container-1)	Probable	NO	NO
All three in same container	Probable	NO	NO
One of the particles in container -0 (container-1)	Probable	YES (NO)	NO (YES)

Table 2.1: The classical and quantum possibilities are tabulated for various arrangements of three particles in two containers. The top two rows correspond to QPHE.

alize QPHE to N particles in $M < N$ containers [2].

Conclusions

Quantum pigeonhole effect is yet another illustration of quantum systems displaying effects beyond the classical predictions. The nonclassical effect in this case emerges as a result of assignment of premeasurement states based on the knowledge of postmeasurement values.

Here we provided the first experimental simulation of QPHE using an NMR quantum simulator. The quantum register consisted of three ^{19}F spins simulating three quantum particles whose intermediate state was probed by a ^{1}H spin (ancilla). The experimental results agreed well with the quantum theoretical predictions. The successful demonstration of QPHE also illustrated good quantum control achieved on a four-qubit heteronuclear NMR system partially oriented in a liquid crystal.

Chapter 3

Steering Quantum Dynamics via Bang-Bang Control: Implementing optimal fixed point quantum search algorithm

In this chapter, I will introduce a novel quantum control technique called Bang-Bang (BB) control (section 2). Then, I will discuss the Optimal Fixed Point Quantum Search (OFPQS) algorithm for finding marked items among unsorted item in section 3 and show how we have experimentally implemented the algorithm on a NMR quantum simulator using the unitary operators realized using BB control (section4). I will also show how to realize certain non-unitary operations using BB control in section 5.

Introduction

Steering a quantum state from one state to another is often required during a quantum simulation and there has been a remarkable progress in the field of quantum control during the past several years (eg. [34, 54, 62, 95, 99]). In most of the previous methods, smooth modulations (SM) of the control parameters is assumed (see Fig. 3.1). Therefore, those require repeated calculation of the unitaries during each segment of the discretized time (see section.2.2 in Chapter 3) in every iteration. Another approach for steering a quantum evolution is based on a sequence of short bursts of full-power control fields. Such an approach, popularly known as a bang-bang (BB) control, has been successfully used in a variety of quantum architectures (for example, [72, 108]). Similar sequences have also been used for controlling spin dynamics. For example, a train of short high-power RF pulses is used to generate a DANTE composite pulse in NMR [11,35,71].

Here we propose a BB control to generate an arbitrary quantum state steering. We also discuss how this scheme scales much more efficiently with the size of the control sequence compared to the SM scheme. Combined with a global optimization routine, this BB scheme can be used to generate not only arbitrary unitaries but also certain nonunitary operations with high fidelities.

Bang-bang approach

Although the following methods can be generalized to other quantum architectures, for the sake of clarity, we shall use the rotating frame picture of an NMR spin system (in an isotropic medium or in a partially oriented medium). Denoting ω_r, J_{rs}, D_{rs} respectively for resonance off-sets, indirect (scalar), and direct coupling constants, and I_r for spin operators, the secular part of the internal Hamiltonian can be written in the form

$$\mathcal{H}_0 = -\sum_r \omega_r I_{rz} + 2\pi \sum_{r<s} (J_{rs} + 2D_{rs}) I_{rz} I_{sz} \tag{3.1}$$

$$+2\pi \sum_{r<s} (J_{rs} - D_{rs})(I_{rx} I_{sx} + I_{ry} I_{sy}), \tag{3.2}$$

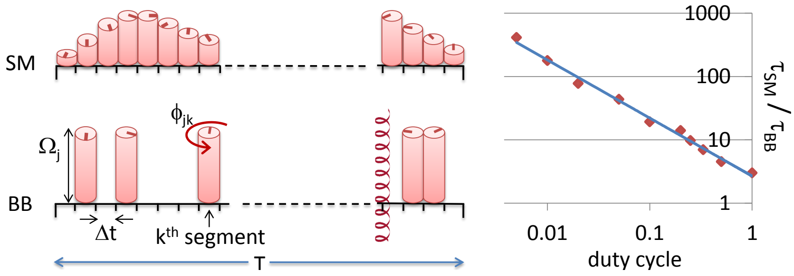

Figure 3.1: Smooth modulation (SM) vs bang-bang (BB) sequence. Ω_j, ϕ_{jk}, Δt are the amplitude, phase, and duration of the segments, and T is the total duration of the sequence. The helix represents the crusher gradient required for nonunitary gates. Performance of BB improves over SM for lower duty cycles as illustrated in the graph. Here τ_{SM} and τ_{BB} indicate respectively SM and BB computational times for calculating 10-qubit propagators of $T = 0.5$ ms duration.

wherein the third term vanishes for weakly interacting spins, particularly for spins belonging to different nuclear species [56].

The BB approach relies on intermittent bursts of full control power instead of its smooth modulation.For generality we consider a spin-system having several nuclear species, and let the jth species be irradiated by an independent RF source with an amplitude switching between either 0 or a maximum value Ω_j, but with a variable RF phase $\phi_j \in [0, 2\pi]$ (see Fig. 3.1). The propagator for the BB sequence can easily be setup by discretizing the total control period T into short segments of duration Δt. Let $\mathbf{S}_j = \sum_m \mathbf{I}_m^{(j)}$ be the collective spin operator of m spins belonging to the jth species. We call $X_j = \exp\{-i(\mathcal{H}_0 + \Omega_j S_{jx})\Delta t\}$ as the basic propagator and it needs to be computed only once. No matrix exponential needs to be calculated during the run-time of iterations, and therefore one obtains a significant speed-up over the SM techniques.

During the kth segment there can be a delay or a pulse. If the kth segment is a delay, then $U_{jk} = \exp(-i\mathcal{H}_0\Delta t)$ is also a constant operator and therefore needs to be evaluated only once. On the other hand, if the kth segment is a pulse with a phase ϕ_{jk}, then the propagator is simply obtained by rotating X_j about the z-axis, i.e., $U_{jk} = Z_{jk} X_j Z_{jk}^\dagger$. Here $Z_{jk} = \exp(-i\phi_{jk} S_{jz})$ is a diagonal operator in the Zeeman product basis and is therefore efficiently evaluated in the run-time of the iterations. The net propagator for the entire control sequence is simply the cumulative product $U = \prod_k \left(\prod_j U_{jk}\right)$.

Typically complex unitaries involving non-local quantum operations require long evolutions under spin-spin interactions, and have low duty cycles. In such cases, the BB approach is orders of magnitude faster than the conventional methods which require repeated matrix exponentiations to evaluate the segment unitaries (Fig. 3.1). If $[\mathcal{H}_0, Z_{jk}] = 0$ (eg. weak-coupling case: $|\omega_r - \omega_s| \gg 2\pi|J_{rs} - D_{rs}|$ for all r and s), then a further speed-up ensues, since the delay propagators become diagonal.

Given a target unitary U_T, we optimize the BB parameters $\{\Omega_{jk}, \phi_{jk}\}$ using the genetic algorithm by maximizing the unitary fidelity F_u. If the goal is to prepare a specific quantum state ρ_T starting from an initial state ρ_in, then we need to calculate the output state $\rho_\mathrm{out} = U\rho_\mathrm{in}U^\dagger$ and the state fidelity

$$F_s = \frac{|\mathrm{Tr}(\rho_T\rho_\mathrm{out})|}{\sqrt{\mathrm{Tr}(\rho_T^2)\mathrm{Tr}(\rho_\mathrm{out}^2)}} \tag{3.3}$$

is to be maximized.

The procedure for using the genetic algorithm is as follows. As indicated in Fig. 1, BB sequence consists of bunches of pulses separated by variable delays. Each bunch of w-pulses is assigned with $w + 1$ genes - one for the number of pulses, and remaining for the phases $\{\phi_w\}$. In order to accommodate variable number of bunches in the pulse sequence, it is necessary to pad the vector with dummy genes which are not necessarily used in the optimization routine. There occurs a delay gene after every bunch of pulses and the delay gene d indicates the number of delays (each of duration Δt) to be inserted between the bunches. Thus the overall gene sequence for two bunches may look like $[w_1$,d_1,w_2,d_2,$\{\phi_1\}$,$\{\phi_2\}]$. All genes, except the phase genes, are rounded to nearest integers. For example, a particular gene sequence $[3, 3, 2, 4, 0, \{0.7, 0.9, 1.2\}, \{0.5, 1.1\}]$ refers to two bunches of pulses containing a sequence of 3 pulses, $3\Delta t$ delay, 2 pulses, $4\Delta t$ delay, and the corresponding phase vectors are $\{0.7, 0.9, 1.2\}$ and $\{0.5, 1.1\}$ respectively. Here 0 is the dummy gene. Genetic algorithm begins with a set of initial gene sequences called population. In every iteration, it picks up the fittest populations and pass onto the next generation. The genetic algorithm seeks to determine an optimal gene-sequence that maximizes the fidelity. We have utilized the genetic algorithm protocol implemented in MATLAB for our optimizations. Here we also note that the genetic algorithm has earlier been used for various optimization purposes in NMR [36, 65].

OFPQS algorithm

Classical search algorithms can find one or more 'marked' items among an unsorted database of Q items in $\mathcal{O}(Q)$ steps. On the other hand, Grover's quantum search algorithm achieves the same task in $\mathcal{O}(\sqrt{Q})$ steps, thereby providing a quadratic speedup over the classical counterpart [42]. Grover's algorithm identifies one of the R marked items among Q unsorted items with the help of a given oracle function that can recognize the marked items. It can also be interpreted as the rotation of an initial state vector $|\psi_Q\rangle$ in the 2D space spanned by the superposition of $Q - R$ non-solution states $|\psi_{Q-R}\rangle$ and the superposition of R solution states $|\psi_R\rangle$ [74]. The Grover iteration thus drives $|\psi_Q\rangle$ towards $|\psi_R\rangle$ in $\mathcal{O}(\sqrt{Q/R})$ steps. However, if we do not know the number of marked items R beforehand, we cannot predict the number of iterations which would land the initial state closest to the marked state. Too few iterations give us a state comprising of mostly non-solution states, whereas, too many iterations can surpass the solution states and we may end up getting non-solution states, yet again. In order to overcome this problem, attempts have been made to develop fixed point quantum search (FPQS) algorithms, which monotonically amplify the probability of obtaining the marked states [43, 96]. While these FPQS algorithms lacked the quadratic speedup, a recent optimal FPQS (OFPQS) algorithm proposed by Yoder *et. al.* achieves this speedup while maintaining the fixed point behavior [103]. In the following we outline

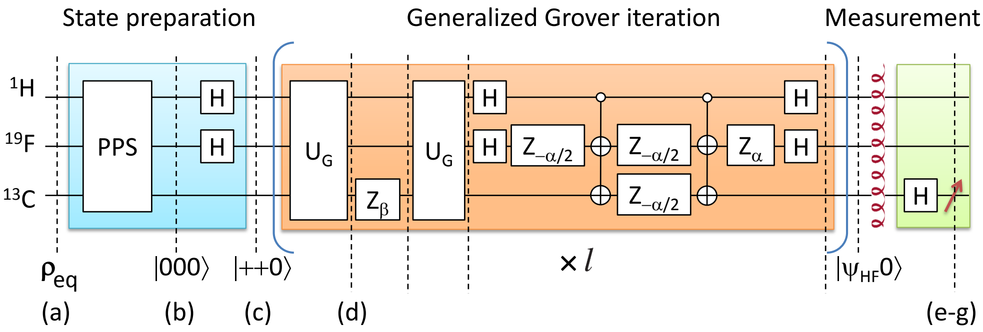

Figure 3.2: Quantum circuit for OFPQS algorithm. Here the angles α and β depend on the iteration number l as indicated in Eqn. 3.4.

the various steps involved in the OFPQS algorithm.

The quantum circuit for the OFPQS algorithm is shown in Fig. 3.2 (for 3-qubits). We need to extract $|\psi_R\rangle$ from $|\psi_Q\rangle$ with a success probability $P_L \geq 1-\delta^2$ for a predefined parameter δ. The algorithm needs a quantum register with a total number of qubits $n \geq \log_2(Q)+1$ including an ancilla qubit, all initialized in the ground state $|0\rangle^{\otimes n}$. The system qubits are then transformed into a uniform superposition by applying $n-1$ Hadamard gates. We are provided with an oracle U_G which when acted upon the marked state, flips the ancilla qubit. Thus, $U_G|\psi_R\rangle|a\rangle = |\psi_R\rangle|a\oplus 1\rangle$ and $U_G|\psi_{Q-R}\rangle|a\rangle = |\psi_{Q-R}\rangle|a\rangle$, where $|a\rangle$ represents the ancilla qubit. Various gates in the generalized Grover iteration are also shown in Fig. 3.2. Let us consider l generalized Grover iterations. Defining $L = 2l+1$ and $\gamma^{-1} = T_{1/L}(1/\delta)$ where $T_L(x) = \cos(L\cos^{-1}x)$ is the L^{th} Chebyshev polynomial of the first kind, the phase rotations are given by

$$\alpha_j = -\beta_{l-j+1} = 2\cot^{-1}\left(\tan(2\pi j/L)\sqrt{1-\gamma^2}\right) \tag{3.4}$$

for all $j = 1, 2, \ldots l$ [103]. As each Grover iterate contains two applications of the oracle U_G, the query complexity is $L-1$.

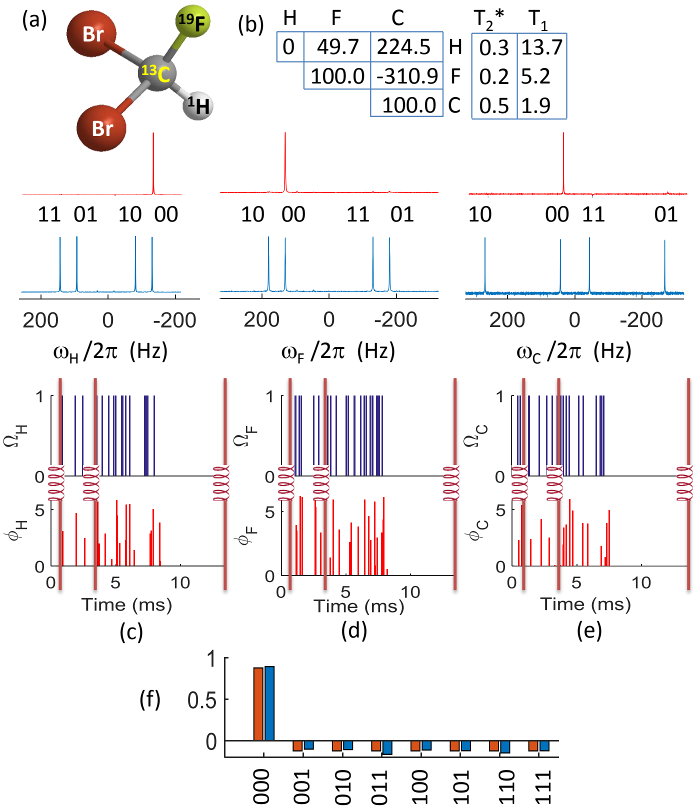

Figure 3.3: (a) Molecular structure of dibromo fluoromethane, (b) the Hamiltonian parameters and relaxation time constants, and (c-e) PPS spectra (upper trace), equilibrium spectra (middle trace), and PPS pulse-sequences (bottom trace) for the ^{1}H, ^{19}F and ^{13}C qubits, (f) bar diagram representing theoretical (red) and experimental (blue) diagonal elements of the traceless deviation density matrix corresponding to $|000\rangle$ PPS. In (b), the diagonal and off-diagonal elements are respectively resonance off-sets and J-coupling constants in Hz.

NMR Implementation

We implement the OFPQS algorithm on a quantum register involving two system qubits ^{1}H and ^{19}F, along with an ancilla qubit ^{13}C of dibromofluoromethane-^{13}C [70] dissolved in acetone-D6 (see Fig. 3.3). All the experiments were carried out on a Bruker 500 MHz NMR spectrometer at an ambient temperature of 300 K. Here, we demonstrate the optimal search algorithm for searching one and two marked items among four unsorted items. As described in the circuit in Fig. 3.2, the experiment mainly involves three stages: (i) preparation of $|000\rangle$ state, (ii) iterations of the generalized Grover operation, and (iii) measurement of the final probabilities using the ancilla qubit. Fig. 3.3 shows the BB-sequence consisting of both RF pulses and crusher gradients automatically generated for the 3-qubit initialization by maximizing the state-to-state fidelity F_s. In the experiment, the crushers are easily achieved using three PFGs whose time instants are obtained by BB optimization scheme. Fidelity of the experimental results of $|000\rangle$ PPS preparation shown in Fig. 3.3 (c-e) is estimated to be 0.998 ± 0.001. Steering the system form thermal state to $|000\rangle$ PPS state causes change in purity hence, it is essentially a non-unitary process. Therefore BB can be also used for realizing non-unitary operations along with crusher gradient and this will be addressed in detail in the next section.

As shown in the circuit of Fig. 3.2, we then prepare the uniform superposition state $|\psi_Q\rangle$ by applying a Hadamard gate on each of the system qubits.

First we divide the circuit shown in Fig. 3.2 into several segments as indicated by the vertical dashed lines. Each of these segments is realized by a BB sequence with an average fidelity of 0.98 over 10% RF inhomogeneity. In order to demonstrate the ability of the BB scheme to realize highly intricate and long circuits, we also implemented the entire generalized Grover iterate (Fig. 3.2) by a single BB sequence. The durations of the BB sequences for $l = \{1, 2, \ldots, 10\}$ varied in the range 40 ms to 220 ms, and consisted of 8,000 to 44,000 segments, each segment being $5\mu s$ long. The simulated

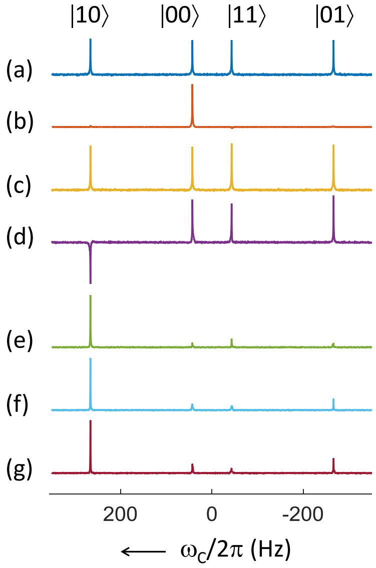

Figure 3.4: The experimental ^{13}C spectra after various steps of OFPQS algorithm as indicated in Fig. 2: (a) equilibrium state, (b) pseudopure state $|000\rangle$, (c) initial state preparation, (d) oracle, (e-g) after amplification with $l = 1,\ 2$, and 3 respectively. Spectra in (a) to (d) are obtained after a Hadamard gate.

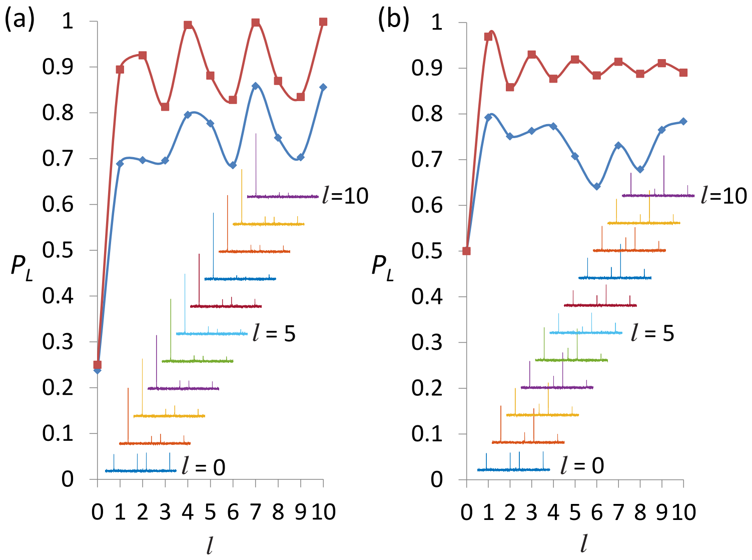

Figure 3.5: The theoretical and experimental results for the probability P_L of finding (a) one ($|01\rangle$) and (b) two ($|10\rangle$ and $|11\rangle$) marked states among four items versus the number of iterations l. The red and blue points respectively represent the theoretically predicted and experimentally obtained probabilities measured directly from the ancilla (^{13}C) spectra (shown in insets).

fidelities were about 0.98 over 10% RF inhomogeneity. While such long sequences implementing multiple control operations are hard to realize by other control methods, the present BB scheme exploits the very low duty-cycle and the one-time evaluation of basic propagators to efficiently compute the overall unitaries. But, all our experiments were performed with formal pulses (where we segregate the circuit into several segments) in order to measure the ancilla spectrum after each stage of the algorithm. We performed the experiments for one ($|10\rangle$) and two ($|10\rangle$ and $|11\rangle$) marked items by systematically increasing the number of iterations (l) in each case.

In order to measure the final probabilities of finding the marked states, we first destroy the coherences by applying a crusher gradient (Fig. 3.2). The relative probabilities of the system qubits being in various eigenstates are encoded in the population differences of the ancilla qubit. Therefore we finally measure the ancilla after applying a Hadamard operator, as shown in Fig. 3.2.

Ancilla measurements

In all our experiments, we set $\delta^2 = 0.2$ so that the theoretical lower bound for the probabilities of finding the marked state is $1-\delta^2 = 0.8$. The spectra obtained at various stages of the algorithm for one marked state, i.e., $|10\rangle$ are shown in Fig. 3.4. The final spectra (e-g) after amplification with $l = 1, 2,$ and 3 clearly identify the marked state with experimental probabilities being in the range 0.7 ± 0.05. Probability of finding the marked items after various iterations are shown in Fig.3.5. The experimental probabilities were in the range 0.75 ± 0.07 and 0.74 ± 0.05 for one and two marked states respectively. The lower values of experimental probabilities are mainly due to pulse imperfections as well as decoherence. In spite of the lower probabilities, the marked states can be clearly identified from the spectra.It is clear that as the number of iterations increases, each final state remains close to the solution state, thus exhibiting the fixed point behavior.

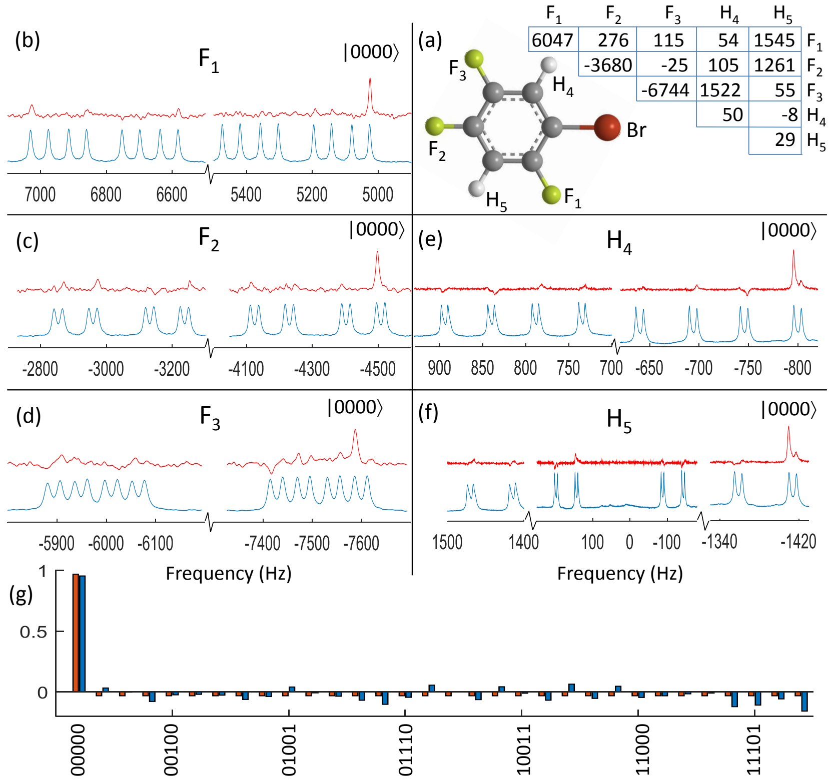

F$_1$	F$_2$	F$_3$	H$_4$	H$_5$	
6047	276	115	54	1545	F$_1$
	-3680	-25	105	1261	F$_2$
		-6744	1522	55	F$_3$
			50	-8	H$_4$
				29	H$_5$

Figure 3.6: (a) Molecular structure of the five-qubit system 1-bromo-2,4,5-trifluorobenzene and its Hamiltonian parameters wherein diagonal and off-diagonal numbers represent resonance offsets and effective (J+2D)-coupling constants (in Hz), (b-f) the spectra corresponding to the thermal equilibrium state (blue) and $|00000\rangle$ PPS prepared from the nonunitary BB sequence (red), and (g) bar diagram representing theoretical (red) and experimental (blue) diagonal elements of the traceless deviation density matrix corresponding to $|00000\rangle$ PPS.

Realizing non-unitary operations using BB

The another important aspect of BB is that it can also be used for realizing certain nonunitary operators along with crusher gradient. In the algorithm, the nonunitary operators are realized by inserting one or more crusher genes. A crusher gene g can take values 0 or 1, corresponding to ON or OFF. $g = 0$ keeps the state unaltered, while $g = 1$ retains only the diagonal elements of the density matrix, thus completely destroying all the coherences.

In this work, we also describe preparing a 3 and 5 qubit PPS target state with the help of a crusher gradient which is essentially a nonunitary operator that attenuates all the coherences, ultimately retaining only the diagonal elements of the density matrix in the computational basis. Simple pulsed-field-gradients (PFGs) used here are efficient in this task unless one generates homonuclear zero-quantum coherences, in which case more advanced twirling methods are needed [6]. Although it is possible to incorporate the effects of decoherence, in our present scheme we ignore such effects by assuming that the control sequences are much shorter than the decoherence time-scales. The PPS spectrum of a 3 qubit PPS and diagonal density matrix obtained after diagonal tomography are shown in Fig.3.3.

To demonstrate the potential of the BB scheme in a larger quantum register, we carried out preparation of pseudopure state in a five-qubit system consisting of three ^{19}F and two ^{1}H spins of 1-bromo-2,4,5-trifluorobenzene (see inset of Fig. 3.6) partially oriented in a liquid crystal [91]. The nonunitary transformation was realized using a single BB sequence of 89.1 ms duration involving four crusher gradients. The normal and PPS spectra of each spin are also shown in Fig. 3.6. The overall fidelity of the PPS preparation was estimated to be 0.96 ± 0.02. The lower fidelity compared to the 3-qubit register is not only due to the increased complexity, but also due to the temporal fluctuations in the dipolar interaction strengths of the 5-qubit system. Nevertheless, the automatic procedure for generating the nonunitary transformation promises applications in a variety of physical implementations involving quantum control.

Conclusions

Bang-bang pulses are efficient to compute, easier to implement, and are robust against pulse errors. Using a nonlocal optimization algorithm, such as the genetic algorithm, it is possible to efficiently optimize the BB sequence to generate any desired unitary transformation or to prepare a quantum state. For example, in the case of NMR, long control sequences are often needed to apply nonlocal transformations. It is unnecessary to apply RF pulses throughout the control sequence, which is not only hard to compute but also prone to RF inhomogeneity errors. The BB control technique allowed us to carry-out the first experimental demonstration of optimal fixed point quantum search algorithm on a three-qubit NMR register. The experimental spectra easily identified the marked state out of a database of four unsorted items.

Combined with crusher gradients it is also possible to realize nonunitary transformations. Using this scheme, we have demonstrated the synthesis and experimental implementation of pseudopure states in 3- as well as 5-qubit NMR quantum registers.

BB sequences can be realized by on and off switching of the control field and therefore it is also applicable to a variety of other architectures where smooth amplitude modulation of control fields is difficult. It may also be possible to realize a hybrid control sequence by combining the BB scheme with other optimal control techniques. Although the present experimental demonstration is in an NMR system, the simplicity of the BB scheme should allow its application in other architectures such as SQUID or NV^- center-based quantum registers.

Chapter 4

Optimized dynamical protection of nonclassical correlation in a quantum algorithm

This chapter focuses on realizing dynamically protected gates by integrating dynamical decoupling (DD) and optimal control techniques. I will also discuss on preserving nonclassical correlations , in particular quantum discord, during Grover's search algorithm by applying dynamically protected gates.

Introduction

Quantum correlations such as quantum discord (QD) and quantum entanglement are regarded as precious resources for QIP [23,30,61]. Hence, it is important to preserve these resources during the process of computation. A quantum register interacts with its environment and suffers loss of information stored in it via decoherence. In practice, another important source of information loss is via incoherence, which results from the spatial inhomogeneity in the control fields [46]. Therefore it is necessary to realize noise-free quantum controls which preserve quantum correlations. Dynamical decoupling (DD) involves modulating the system-environment interaction and thereby suppress decoherence as well as incoherence [97, 98]. It usually consists of a sparse sequence of instantaneous qubit-flips to systematically modulate the system-environment interaction. Unlike the fault-tolerant schemes based on error-correction or decoherence-free subspaces, DD requires no additional resource in terms of ancillary registers [58, 93, 94]. Accordingly, DD has been widely studied and implemented experimentally [3,5,80,86]. Recently several experimental studies have been performed towards protecting quantum correlations in quantum memory [52, 92]. More recently, combining DD and quantum gates had been studied theoretically [55] as well as experimentally [83, 106, 107].

In this work, we incorporate DD within the optimal control procedure, which not only avoids the manual slicing of the gate segments, but also naturally takes care of DD pulse-errors. In particular, we demonstrate realizing protected gates by combining DD and Gradient Ascent Pulse Engineering (GRAPE) protocol [54]. As a specific case, we study the experimental efficiency of protected gates implementing Grover's search algorithm in terms of preserving QD and of maintaining the probability of marked state.

Dynamically protected gates

Theory

In this subsection, I shall discuss the theoretical description of DD protected gate. Let us consider an N-spin system with an internal Hamiltonian $\mathcal{H}_S$ and a control Hamiltonian

$$\mathcal{H}_C(t) = \sum_{i=1}^{N} \Omega_x(t) I_{ix} + \Omega_y(t) I_{iy} \tag{4.1}$$

where $\Omega_x(t)$ and $\Omega_y(t)$ represent the x and y components of the amplitude and phase modulated RF fields being applied on all the spins. Simultaneously, let us also consider the system-environment interaction Hamiltonian $\mathcal{H}_{SE}(t)$, so that the total Hamiltonian is of the form

$$\mathcal{H}(t) = \mathcal{H}_S + \mathcal{H}_C(t) + \mathcal{H}_{SE}(t). \tag{4.2}$$

While the system-environment interaction Hamiltonian $\mathcal{H}_{SE}$ that is responsible for the decoherence, is usually hard to characterize, it is still possible to minimize it's disruptive effect by controlled system modulations. The goal here is to achieve a quantum operation while protecting the quantum register against the environmental decoherence. In the following, we first describe the procedure for integrating DD with Quantum Control (QC) to achieve a protected quantum operation.

Suppose a propagator U_T is to be realized by the control fields $\{\Omega_x(t), \Omega_y(t)\}$. In practice, time-discretized (piecewise constant) amplitudes are used, i.e., during the kth segment $[(k-1)\Delta t, k\Delta t]$, the control parameters are $\{\Omega_{x,k}, \Omega_{y,k}\}$ (see Fig. 4.1). The ideal closed-system unitary for the kth segment is

$$u_k = \exp\left[-i(\mathcal{H}_S + \mathcal{H}_{C,k})\Delta t\right], \tag{4.3}$$

where $\mathcal{H}_{C,k} = \sum_i \Omega_{x,k} I_{ix} + \Omega_{y,k} I_{iy}$. The control propagator for a sequence of n-segments is $U = u_k u_{k-1} \cdots u_1$.

In the presence of environmental interaction however, the actual open-system propagator for the k-th segment becomes

$$u_k^{\mathrm{op}} = \exp\left[-i(\mathcal{H}_S + \mathcal{H}_{C,k} + \mathcal{H}_{SE})\Delta t\right], \tag{4.4}$$

which acts on the joint system-environment state. Subsequent tracing out of the environmental part results in decoherence of the quantum system. DD pulses modulate the system-environment evolution and thereby suppress decoherence.

The propagator for a DD pulse with flip-angle β and phase α is given by $P_{\beta,\alpha} = \exp(-i\beta S_\alpha)$, where $S_\alpha = \sum_i I_{ix} \cos\alpha + I_{iy} \sin\alpha$. The overall propagator for a protected sequence consisting of M DD pulses sandwiched between control propagators is (see Fig. 4.1),

$$U_P = U_{M+1} \prod_{j=1}^{M} P_{\beta_j,\alpha_j} U_j. \tag{4.5}$$

Using the toggling-frame picture [45, 106], we may rewrite the above in the form,

$$U_P = U_{M+1} \prod_{j=1}^{M} \tilde{U}_j, \tag{4.6}$$

where the toggling frame unitaries $\tilde{U}_j = T_j^\dagger U_j T_j$, and $T_j = P_{\beta_{j-1},\alpha_{j-1}} P_{\beta_{j-2},\alpha_{j-2}} \cdots P_{\beta_1,\alpha_1}$ and $T_1 = T_{M+1} = \mathbb{1}$. Given a target propagator U_T, we optimize the control amplitudes which maximize the fidelity

$$F(U_P, U_T) = \mathrm{Tr}\left[U_T^\dagger U_P\right] / \mathrm{Tr}\left[U_T^\dagger U_T\right]. \tag{4.7}$$

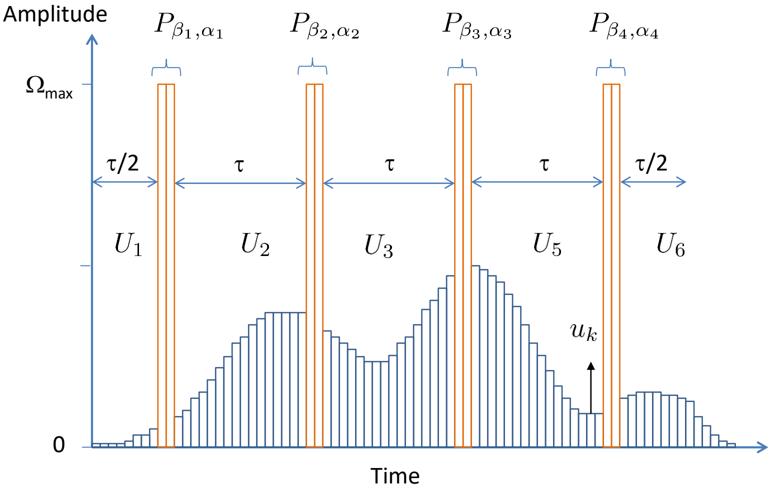

Figure 4.1: Protected quantum gate scheme. Certain segments are reserved for the full-amplitude ($\Omega_{\max}$) DD-pulses (P_{β_j,α_j}) and other segments are subject to optimization to realize a given target unitary U_T.

Unlike the previous works on the protected gates [106, 107], where $\beta = \pi$ was used, in this work we generalize to variable DD flip angles. We also integrate periodic, full-amplitude, DD pulses in the optimal control procedure itself, by pre-assigning segments and freezing their amplitudes and phases. The main advantage of this method is that the DD pulses along with their imperfections, like additional spin-flips, RF inhomogeneity, and offset errors, are accounted and corrections are incorporated by the control segments in order to achieve a robust sequence for implementing the target propagator. Moreover, there is no need for the manual slicing of control pulses to introduce DD pulses. In the following, we shall consider the dynamical protection of a single qubit and illustrate how it can be achieved by DD pulses with a range of flip-angles.

A simple model:

Protected NOT gate on a single qubit

For a simple demonstration of dynamical protection, we choose the NOT gate, $U_T = \exp(-i\pi I_x)$ on a single qubit. We consider a DD pulse $P_{\beta,x} = \exp(-i\beta I_x)$ sandwiched between two identical effective control propagators $U = \exp(-i\pi/2\ I_x)$, such that the total propagator $U_P = UPU$. Here the DD pulse has not been accounted by the control propagators, and therefore the fidelity $F(U_P, U_T) = \cos(\beta/2)$ drops with the flip-angle. In order to account for the DD pulse, we introduce a correction in the control propagator such that $U_c = \exp\{-i(\pi/2 - c)I_x\}$, where c is the correction factor. In this case, fidelity of the target with the net corrected propagator $U_{Pc} = U_c P_{\beta,x} U_c$ becomes $F(U_{Pc}, U_T) = \cos(\beta/2 - c)$. Thus setting $c = \beta/2$ leads to unit fidelity for arbitrary DD flip-angles. We now consider an undesired offset-error ϕ_z such that the DD-corrected control propagators take the form $U_{cz} = \exp[-i\{(\pi/2 - \beta/2)I_x + \phi_z I_z\}]$, then the fidelity of the operation $U_{Pcz} = U_{cz} P_{\beta,x} U_{cz}$ becomes

$$F(U_{Pcz}, U_T) = \left(\frac{4\phi_z^2}{\gamma^2} + \frac{\eta^2}{\gamma^2}\cos\frac{\gamma}{2}\right)\sin\frac{\beta}{2} + \frac{\eta}{\gamma}\sin\frac{\gamma}{2}\cos\frac{\beta}{2}, \tag{4.8}$$

where $\gamma^2 = \eta^2 + 4\phi_z^2$ and $\eta = \pi - \beta$. Clearly $F(U_{Pcz}, U_T) = 1$ for $\beta = \pi$. However, for small values of ϕ_z, $F(U_{Pcz}, U_T) \approx 1$ for all values of β. Without the DD pulse, the fidelity of the unprotected operation $U_z^2 = \exp\{-2i(\pi/2\ Ix + \phi_z I_z)\}$ is $F(U_z^2, U_T) = \frac{\pi}{\gamma}\sin\frac{\gamma}{2}$, which starts from unity for $\phi_z = 0$, but drops as ϕ_z starts increasing. Fig. 4.2(a) displays the relative performances of these DD sequences with respect to the offset-error ϕ_z. For this simple model, it turns out that while $\beta = \pi$ works the best, even $\beta = \pi/2$ can show significant protection.

We now consider a more general case of a XY-DD protected NOT gate $U_{cz}^{(y)} P_{\beta,y} U_{cz}^{(y)} U_{cz}^{(x)} P_{\beta,x} U_{cz}^{(x)}$, where

$$U_{cz}^{(x/y)} = \prod_{j=1}^{n} \exp\left\{-i\left(\frac{\pi}{4n} - c_{x/y} I_x - d_{x/y} I_y + \phi_z \eta_j\right)\right\}$$

subjected to a random noise in the range $[-\phi_z\eta_j, +\phi_z\eta_j]$ with a variable amplitude ϕ_z. We have studied the above gate with $n = 100$ segments and numerically optimized the correction factors $c_{x/y} I_x$ and $d_{x/y}$. During the above optimization, noise term $\phi_z\eta_j$ need not be considered. The contour plot of the fidelity of such an XY-DD protected NOT gate is shown in Fig. 4.2(b). For the unprotected NOT gate, the fidelity drops below 0.9 for $\phi_z > 3°$ as shown by the dashed line. However in this region, fidelity of the protected NOT gate is above 0.99 for a wide range of DD angles. These models indicate that unlike the coherence storage schemes where $\beta = \pi$ is usually considered, protected quantum gates can also be constructed out of $\beta \neq \pi$.

Before we discuss the experimental and numerical studies, we first briefly review quantum discord and its evolution during different stages of Grover's algorithm.

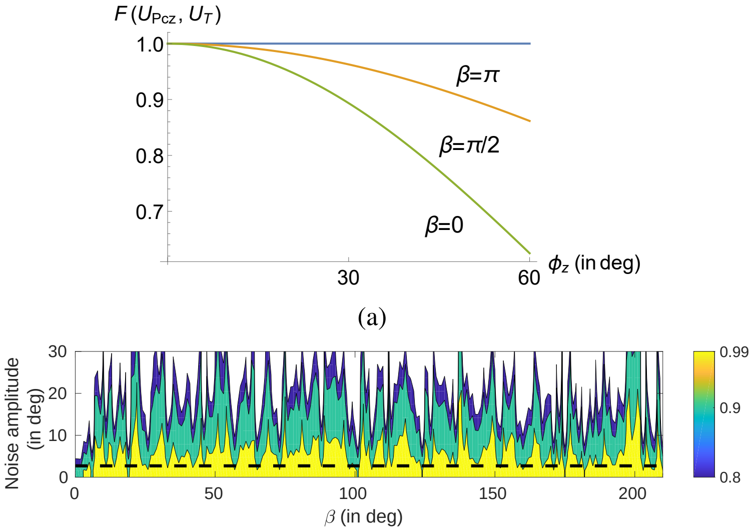

(a)

(b)

Figure 4.2: (a) Fidelity of the protected NOT gate versus offset error (in deg) corresponding to the DD sequences $U_{Pcz} = U_{cz} P_{\beta,x} U_{cz}$. (b) Fidelity of the protected NOT gate $U_{cz}^{(y)} P_{\beta,y} U_{cz}^{(y)} U_{cz}^{(x)} P_{\beta,x} U_{cz}^{(x)}$ versus DD angle β and amplitude of the random phase-rotations. For the unprotected NOT gate, the fidelity drops below 0.9 for the noise amplitude $\phi_z > 3^\circ$ as indicated by the dashed line.

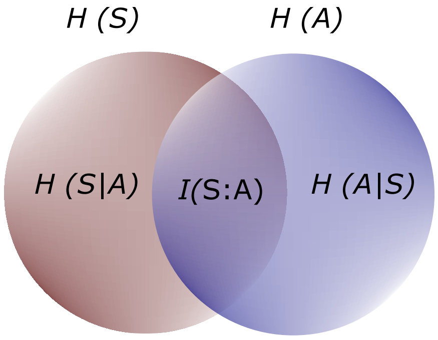

Figure 4.3: Venn diagram representing the total information $H(S, A)$ of a bipartite system. $H(A)$ and $H(S)$ are individual information of the system A and S respectively, $I(S : A)$ is the mutual information and $H(S|A)$ and $H(A|S)$ are conditional entropies.

Quantum Discord (QD)

Quantum entanglement is considered as an important resource in QIP [8, 82]. Even when the entanglement is absent, a bipartite quantum system (S, A) may possess another useful type of quantum correlation known as quantum discord (QD) [76]. QD is quantified by the minimal mismatch between the mutual information obtained in two classically equivalent, but quantum mechanically distinct ways. As can be seen from Fig. 4.3, the mutual information can be expressed either as

$$I(S:A) = H(A) + H(S) - H(S,A), \tag{4.9}$$

or as

$$J(S:A) = H(S) - H(S|A). \tag{4.10}$$

In classical information,

$$H(X) = -\sum_x p_x \log_2 p_x \tag{4.11}$$

is the Shannon entropy obtained using the probabilities p_x of xth outcome. Similarly, the joint entropy

$$H(S,A) = -\sum_{a,s} p(s,a) \log_2 p(s,a), \tag{4.12}$$

is obtained using the joint probabilities $p(s,a)$ and the conditional entropy

$$H(S|A) = -\sum_{a,s} p_a p(s|a) \log_2 p(s|a), \tag{4.13}$$

is obtained using the conditional probability $p(s|a)$, which is the probability of occurrence of outcome s given that the outcome a has occurred.

In quantum information, we replace the Shannon entropy with von Neumann entropy, i.e.,

$$H(\rho_X) = -\sum_x \lambda_x \log_2(\lambda_x), \tag{4.14}$$

where λ_x are the eigenvalues of the density matrix ρ_X. The joint von Neumann entropy $H(S, A)$ is evaluated using the eigenvalues $\lambda_{s,a}$ of the full density matrix $\rho_{S,A}$. On the other hand, the conditional entropy $H_{_\Pi}(S|A)$ is evaluated using the eigenvalues $\lambda_{s|a_\Pi}$ of the post-measurement density matrix $\rho_{S|A_\Pi}$ after carrying out a measurement along a basis $\{\Pi_i^a\}$.

While the two forms $I(S : A)$ and $J(S : A)$ of mutual information are identical in the classical case, the requirement of measurement for the latter form makes them different in the quantum case. This difference, when minimized over the entire set of orthormal measurement bases $\{\Pi\}$, is often nonvanishing, and is attributed to a form of quantum correlation termed as quantum discord (QD) [60, 76], i.e.,

$$D(S|A) = I(S : A) - \max_\Pi J(S : A). \tag{4.15}$$

Since QD is also regarded as an important resource for quantum computing, it is necessary to understand its evolution during quantum algorithms. In the following we discuss the evolution of QD in Grover's search algorithm.

QD in Grover's algorithm

Grover's algorithm identifies a marked item in an unsorted database of N items in $O(\sqrt{N})$ iterations, while a classical algorithm needs $O(N)$ iterations on an average.

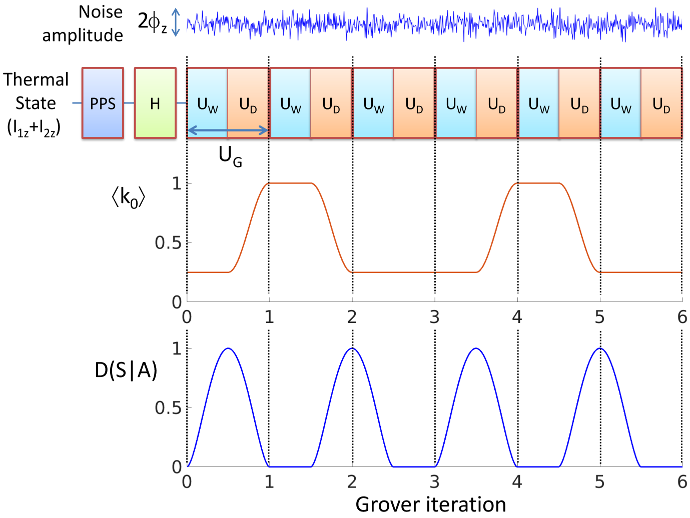

Figure 4.4: Various experimental stages of Grover's search algorithm for up to six iterations subjected to a random noise (top trace). It begins with a thermal initial state, followed by preparation of pseudopure state (PPS), Hadamard operator (H), and application of Grover's iterates (U_G) consisting of oracle (U_W) and diffusion (U_D) operators. The middle and bottom traces show ideal evolutions of probability of marked state $\langle k_0 \rangle$ and QD respectively.

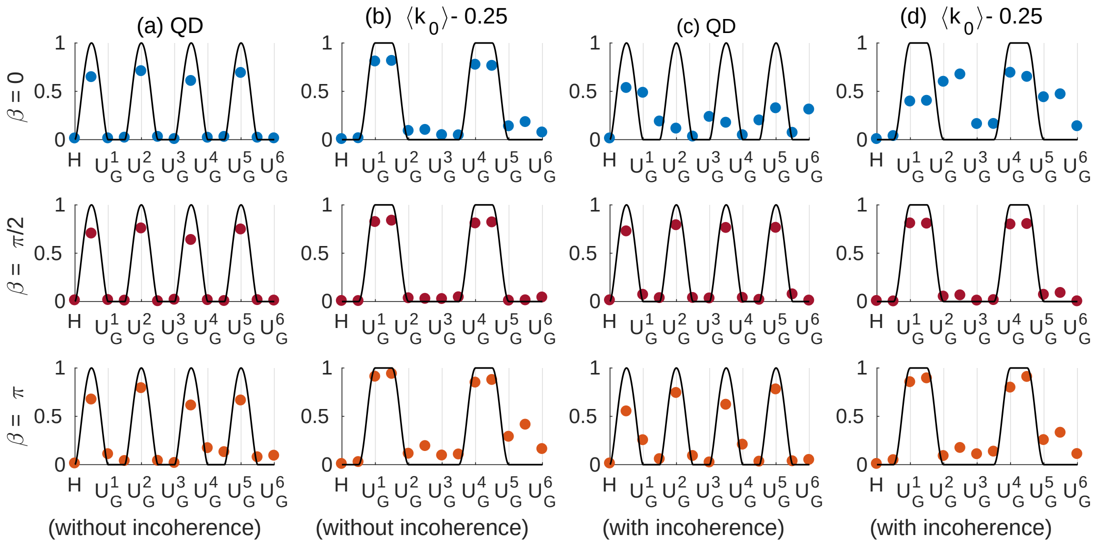

Figure 4.5: Idealized estimations (solid lines) and experimental (filled circles) QD (in units of $\epsilon^2/\ln 2$) (a, c) and probability $\langle k_0 \rangle - 0.25$ (in units of ϵ; constant 0.25 is due to the traceless deviation matrix experimentally estimated) of the marked state (b, d) under Grover iterates with XY DD-protections without (a, b) and with (c, d) additional incoherence. The top trace ($\beta = 0$) corresponds to unprotected Grover iterates. The middle ($\beta = \pi/2$) and the bottom ($\beta = \pi$) traces correspond to XY DD protected Grover iterates.

The algorithm starts with initializing a quantum register into an uniform superposition

$$|\psi_0\rangle = \frac{1}{\sqrt{N}} \sum_{k=0}^{N-1} |k\rangle. \tag{4.16}$$

It then uses an oracle

$$U_W = \sum_{k=0}^{N-1} (-1)^{\delta_{k,k_0}} |k\rangle\langle k| \tag{4.17}$$

that flips a marked state $|k_0\rangle$, and a diffusion operator

$$U_D = 2|\psi_0\rangle\langle\psi_0| - \mathbb{1}, \tag{4.18}$$

which inverts each of the basis states about the mean. Together these two operations constitute a Grover's iterate, i.e., $U_G = U_D U_W$, that amplifies the marked state amplitude.

The top trace of Fig. 4.4 displays various stages in the Grover's algorithm up to six iterations. The middle trace displays the periodic evolution of the probability $\langle k_0 \rangle$ of the marked state $|k_0\rangle = |01\rangle$. The bottom trace displays the corresponding evolution of QD over six iterations. As expected, QD vanishes whenever the system reaches the marked state - which is a classical state. QD vanishes also for uncorrelated states of the form $\rho_S \otimes \rho_A$ not involving mutual interaction between S and A. The question that we ask is, how does QD evolve in a noisy channel implementing Grover's algorithm, and how well it can be protected by interleaving the Grover's iterates with DD. In the following section, we explore the answer to the above question by NMR based experiments.

Experiments

In our NMR experiments we utilize the two spin-1/2 proton nuclei of Cytosine dissolved in deuterated dimethylsulfoxide (DMSO-D$_6$). All the experiments are carried out on a Bruker 500 MHz NMR spectrometer at an ambient temperature of 300 K. The resonance offsets of the two protons are 436 Hz and -436 Hz, while the scalar coupling constant $J = 7.0$ Hz. Starting from the thermal equilibrium state $I_{Sz} + I_{Az}$, we use the spatial averaging technique [22] to prepare the pseudopure state (PPS) $(1-\epsilon)\mathbb{1}/4 + \epsilon|00\rangle\langle 00|$, where $\epsilon \sim 10^{-5}$ is the purity factor typically present in NMR systems.

We generated the DD-protected oracle operator U_W corresponding to the marked state $|k_0\rangle = |01\rangle$ and the diffusion operator U_D by incorporating DD pulses into the GRAPE optimal control technique [10, 54] as described in section II. Each GRAPE segment was of duration 5.1 μs. The fidelities of these GRAPE pulses, each about 75 ms long, were above 0.99 after averaging over 10% RF inhomogeneity distribution. A full power DD pulse was introduced in between every 1000 segments. The phase α of the DD pulses was alternated between x and y.

To estimate QD, we need to obtain the density matrix at various stages of Grover's algorithm (see Fig. 4.4). The density matrix is generally obtained using quantum state tomography (QST) which involves a set of independent experiments (on identically prepared states) each measuring a particular set of observables. The expectation values are then obtained by measuring the signal intensities. We have adopted a QST procedure that results in only absorptive spectral lines which precisely quantify the expectation values without requiring any further numerical processing.

Pure-phase Quantum State Tomography

In the conventional scheme (like the ones mentioned in [74], [84], [90]), one obtains absorptive, or dispersive, or even mixed-phase spectral lines which are often hard to quantify. A pure-phase tomography has been designed to obtain only absorptive spectral lines which are far easier and precise to quantify. In the case of a two-qubit homonuclear system involves a set of six experiments:

$(i)\quad \triangleright \equiv G_z - 60_{90} - \tau$

$(ii)\quad 75_{-180} - \triangleright$

$(iii)\quad 75_{105} - \triangleright$

$(iv)\quad 1/2J - 75_{30} - \triangleright$

$(v)\quad 5/12J - 75_{105} - \triangleright$

$(vi)\quad 75_{195} - 5/12J - 75_{15} - \triangleright.$

Here G_z is the pulsed-field gradient to destroy the coherences, τ is the delay optimized to suppress the homonuclear zero-quantum coherence, and J is the indirect spin-spin coupling constant. Four absorptive transitions obtained after each of the above experiments are integrated and the density matrix is estimated using the constraint-matrix procedure described in [84, 90].

Results and Discussions

After obtaining the experimental density matrix ρ_{exp}, we estimated QD via the optimal set of measurement bases proposed by Lu et al. [60]. Similarly, we also estimated the probability $\langle k_0 \rangle = \langle k_0 | \rho_{\text{exp}} | k_0 \rangle$ of the marked state for $|k_0\rangle = |01\rangle$. Fig. 4.5 (a) displays experimentally estimated QD values (in units of $\epsilon^2/\ln 2$) at various stages of the Grover's algorithm for up to six iterations, with unprotected (top trace) as well as for XY DD-protected Grover's iterates with $\beta = \pi/2$ (middle trace) and $\beta = \pi$ (bottom trace). Fig. 4.5 (b) displays the corresponding probability of the marked state $|01\rangle$. Thus, in the absence of incoherence, we observed that the experimental values are in reasonably good agreement with the idealized predictions represented by solid lines (also described in Fig. 4.4) indicating high-quality of quantum controls as well as low inherent noise in the NMR system.

To further investigate the power of DD protection, we deliberately introduced incoherence in the form of linear static-field inhomogeneity along the z-axis by using approximately 5 mG/cm pulsed-field-gradient (PFG). It introduces a differential offset of ± 10 Hz across the sample volume corresponding to a phase shift $\phi_z \sim 0.1^\circ$ during a single GRAPE segment of duration 5.1 μs. The total duration for six Grover-iterations was about 0.9 second, and the translational diffusion of the molecules over this period further introduces randomness in the overall dephasing. The top trace of Fig. 4.5 (c,d) display respectively the experimentally measured QD values and probabilities with unprotected Grover iterates in the presence of such an incoherence. Clearly, the experimental data without DD protection show little correlation with the ideal trajectories. The other traces of Fig. 4.5 (c,d) display the experimental data under XY DD-schemes with $\beta = \pi/2$ and $\beta = \pi$ as indicated. The best protection was achieved by the XY DD sequence consisting of $\pi/2$ pulses.

The bars with solid edges in Fig. 4.6 show the average root-mean-square (RMS) deviation of the experimental QD (a) and probabilities $\langle k_0 \rangle$ (b) from the idealized theoretical values displayed in Fig. 4.5 for various DD flip angles without (open bars) and with (filled bars) incoherence. In general, RMS deviations are enhanced by incoherence, but suppressed by DD. Interestingly, the DD protection with $\beta = \pi/2$ showed the best performance in suppressing the effects of incoherence. To further strengthen this claim, we simulated RMS deviations using GRAPE pulses corresponding to U_{PG} for six iterations with 20% inhomogeneous RF fields and incoherent fields ranging from -10 Hz to $+10$ Hz. The results are shown by bars with dashed edges in Fig. 4.6 (a,b). The simulations also support the experimental finding that $\beta = \pi/2$ DD protection has a superior performance. We also estimated the mean fidelities $F_m = \frac{1}{6}\sum_{j=1}^{6} F(U_{PG}^j, U_G^j)$ (see Eq. 4.7) as displayed in Fig. 4.6 (c). All the mean fidelities have good values in

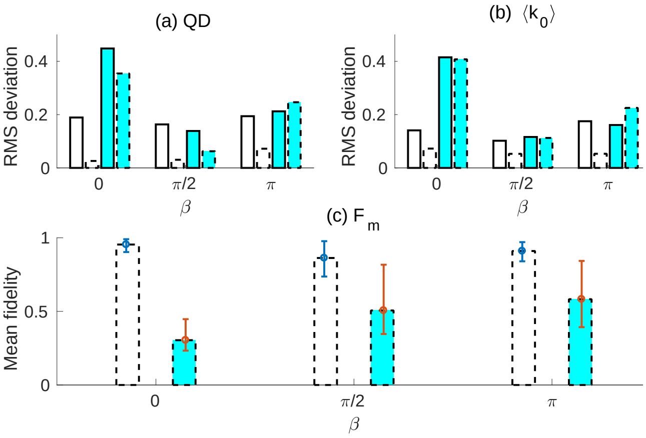

Figure 4.6: Average root-mean-square deviation (bars with solid edges) between the experimental data and ideal theoretical values (shown in Fig. 4.5) for QD (in units of $\epsilon^2/\ln 2$) (a) and the probability $\langle k_0 \rangle$ (in units of ϵ) (b) of marked state versus DD flip angle β without incoherence (open bars) and with incoherence (filled bars). The corresponding numerical simulations are shown by bars with dashed edges. (c) Numerically estimated fidelities of U_G averaged over six iterations without (open bars) and with (filled bars) incoherence. Here errorbars indicate variations over six iterations.

the absence of incoherence again indicating a good control. However in the presence of incoherence, while the unprotected iterate completely fails, both $\beta = \pi/2$ and $\beta = \pi$ cases show relatively better performances.

We now try to understand the correlation between probability of the marked state and QD. Fig. 4.7 displays the experimental QD values versus the probabilities without (a) and with (b) incoherence. Ideally, the initial superposition state has no QD, but has same probability of 0.25 for all the four basis states, which corresponds to the bottom left corner as indicated by the dashed line. The intermediate state after the oracle U_W takes the superposition to a highly correlated state with a maximum QD, but still without any higher probability for the marked state, which corresponds to the bottom-right corner. Diffusion operator then amplifies the probability of the marked state, which is a classical state with no QD, and therefore corresponds to the top-left corner. In the case of no incoherence, most of the data points are localized to the expected corners. However, in the presence of incoherence, while there is a significant dispersion of data points

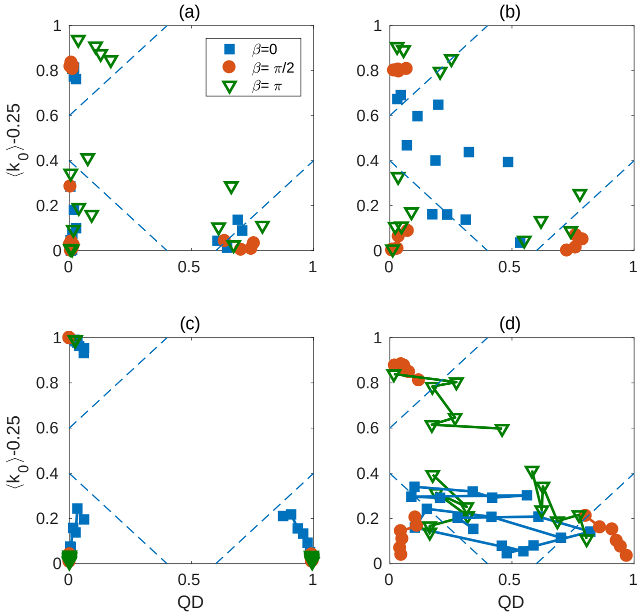

Figure 4.7: Experimental values of QD for six Grover iterations plotted against the probability $\langle k_0 \rangle - 0.25$ without (a) and with (b) incoherence. Simulated values of QD versus probability for 10 Grover iterations without (c) and with (d) incoherence. In all the cases, QD values are in units of $\epsilon^2 / \ln 2$ and probability values are in units of ϵ.

belonging to the unprotected gates ($\beta = 0$), those belonging to protected gates ($\beta \neq 0$) still maintain localization. Thus DD schemes preserve quantum correlations and thereby assure success of the algorithm. Here again $\beta = \pi/2$ shows the best performance. Figures 4.7 (c,d) display the simulated values of probability versus QD without (c) and with (d) incoherent fields (ranging from -10 Hz to $+10$ Hz) for 10 Grover iterations. In the absence of incoherence there is a reasonable localization for all the three values of β. However, with incoherence the unprotected Grover iterations completely fail since the maximum probability of the marked state remained less than 0.4 throughout the iterations. The data points corresponding to protected Grover iterates with $\beta = \pi$ are significantly dispersed, but still show signatures of localization, while those with $\beta = \pi/2$ show the best localization consistent with the experimental results.

Conclusions

Quantum correlations such as quantum discord and quantum entanglement form resources that fuels quantum information processors. In this work, we experimentally studied the evolution of quantum discord as well as the probability of a marked state over six iterations of Grover's quantum search algorithm on an ensemble of spin-1/2 nuclear pairs using nuclear magnetic resonance methods. Unlike the earlier works on protected quantum gates which considered only π pulses, we have generalized to DD-pulses with variable flip angles. Further, we have integrated the dynamical protection into GRAPE optimal control protocol by pre-assigning the positions of dynamical flips. In this way, protected quantum gates are robust by construction against the external noise. Similar protocol can also be incorporated in other optimal control techniques such as Bang-Bang [9], Krotov [67], etc. While the protected gates performed generally better, to investigate the extent of protection, we introduced an additional incoherent noise in the form of a pulsed field gradient. In this case, we observed a significant benefit of dynamically protected gates. Interestingly, we found that the dynamical protection with $\pi/2$ flip-angles to outperform those with π. We have supported our experimental findings with numerical simulations and also provided simple single-qubit models to explain this observation. Although, DD with non-inversion pulses might appear counter intuitive at the outset, $\pi/2$-rotation based modulation schemes such as WAHUHA [39] and solid-echo sequences [45] have long been used in NMR spectroscopy. We believe that our study will be useful in understanding dynamical protections and thereby designing robust quantum controls.

Part - II

Chapter 5

Nitrogen-vacancy Centers in diamond

This part of my thesis focuses on building experimental platform for performing quantum information processing using Nitrogen-vacancy (NV) centers in diamond. This chapters discusses the fundamental properties of the NV center in diamond.

Introduction

Nuclear magnetic resonance (NMR) is a powerful technique for obtaining structure and dynamics of molecules in chemistry. It also got high importance in medical applications, namely, the magnetic resonance imaging (MRI) [63]. However, NMR is not so promising as a quantum computer as it is an ensemble based quantum processor. The NMR quantum register is in a statistical mixture of all possible states in thermal equilibrium and it is difficult to initialize them in a pure state under ambient conditions. It often requires extreme conditions such as high magnetic field and cryogenic temperature. Besides, scalability is a challenge in NMR as it is not possible to find molecules with large number of NMR active nuclei in nature.

Nitrogen-Vacancy (NV) centers in diamond has recently emerged as a promising candidate for quantum information processing. The electronic spin states of the NV center can be initialize with a purity better than 99% through off resonant optical pumping and resonance fluorescence can be exploited to detect the electronic spin state of the NV center even at room temperature [19, 27, 101].

Diamond

Diamond is known as the hardest naturally occurring substance found on Earth. It is one of the allotropes of carbon where four sp^3 hybridized adjacent carbon atoms are bounded via covalent bonds with a bonding angle of 109.5°. The unit cell consists of two face-centered-cubic (fcc) Bravais lattices, which are displaced by a/ 4 (1, 1, 1), where $a = 3.57A^\circ$ is the lattice parameter and the distance between neighboring carbon atoms is of $d = 1.44A^\circ$.

Diamond is an insulator with a band gap of 5.45 eV and the corresponding wavelength is in the ultraviolet range. Therefore, diamond transmits visible light and appears transparent. However, the defects in the diamond lattice introduces extra band gaps between the valence and conduction bands of the diamond and consequently appears colorful.

The diamond is naturally grown in the mantle of earth where it has the favorable conditions to grow such as the pressure in the range of 7-8GPa and the temperature ranging from 1400 to 1600°. Under ambient conditions, diamond is not a stable allotrope of carbon but graphite. Even though, diamond to graphite conversion process is a rather slow due to high energy barrier of about $728KJ/mol$ under ambient conditions [102].

Many efforts have been made for growing diamonds in lab due to their special properties. And, now, diamonds can be grown in laboratories by creating the growth conditions. The most common techniques for growing diamonds are High Pressure High Temperature (HPHT) and chemical vapour deposition (CVD).

High Pressure High Temperature (HPHT) growth

HPHT diamonds are subjected to extremely high temperature (>2000°C) and pressure ($\approx 10GPa$) inside special chambers in a lab in order to recreate the process that takes place in the mantle of earth. The phase transition from graphite to diamond is allowed under these conditions. This method is highly used in jewellery industries as it incorporate large amount of impurities such as Nitrogen and Boron during the growth. For example, introducing nitrogen during the growth turns the diamond yellow. Diamonds can be classified in to four types depending up on the amount of Nitrogen and Boron impurities [14, 105].

- **Type Ia**: This type of diamonds contain Nitrogen ($< 3000ppm$) in large clusters throughout the crystal lattice.
- **Type Ib**: These diamonds contain single nitrogen ($< 500ppm$) atoms instead of clusters dispersed throughout the crystal lattice.
- **Type IIa**: Low nitrogen ($< 1ppm$) content.
- **Type IIb**: Low nitrogen ($< 1ppm$) content as in type IIa but boron impurities.

Chemical Vapour Deposition (CVD)

CVD and particularly microwave plasma-activated CVD is another popular method for growing synthetic diamond. This method requires a diamond seed crystal placed inside a growth chamber which is at a pressure of about 10's of mbar and temperature in the range of 700-1200°C. The surface of the diamond seed crystal serves as a growth substrate. It mainly consists of a gas mixture of Hydrogen and a small amount of Carbon containing gas such as Methane(CH_4) which is heated up by microwave irradiation and eventually becomes a plasma. The Hydrogen atoms serve the process mainly in two ways. Firstly, the diamond lattice is stabilized and prevented from the formation of graphite by termination with hydrogen atoms. Secondly, the gaseous activation process dissociates the molecular hydrogen into atoms which leads to the formation of reactive Carbon-containing radicals such as CH_3 radicals by reacting with the source hydrocarbon. These Hydrogen atoms also remove the Hydrogen from the surface CH bonds and create surface radical sites. These radical sites often get reacted with the gas phase Carbon containing radicals hence, result the diamond growth. The complete details of this process can be found in Ref. [16]. The colored diamond can be grown by doping with Nitrogen or Boron impurities. These color centers can also be created through irradiation process after the synthesis.

Color Centers in Diamond

Over 500 luminescent centers are found in diamond. Those are mainly due to additionally incorporated atoms such as Silicon or Phosphorous or just due to missing carbon atoms. Such defects introduce additional energy levels between valence and conduction band of the diamond which are of 5.47 eV apart. Consequently, additional transitions are allowed with transitions frequencies in the visible light range. NV^- center is one of that kind. NV^- centers have recently gain more popularity due to their applications in quantum sensing, quantum information processing and metrology. This the following section, I am going to briefly discuss the electronic and spin properties of the NV^- center in diamond.

Nitrogen-Vacancy Center

NV center is a point defect in diamond consists of substitutional Nitrogen atom with an adjacent vacancy. Together with the three sp^3 neighbor Carbon atoms which forms a tetrahedral structure resulting a C3v symmetry with the Nitrogen atom and the vacancy lying on the symmetry axis (NV axis). Owing this symmetry, it can have four different orientation, namely along the four crystallographic axes$[111]$, $[\bar{1}\bar{1}1]$, $[1\bar{1}\bar{1}]$ and $[\bar{1}1\bar{1}]$ as

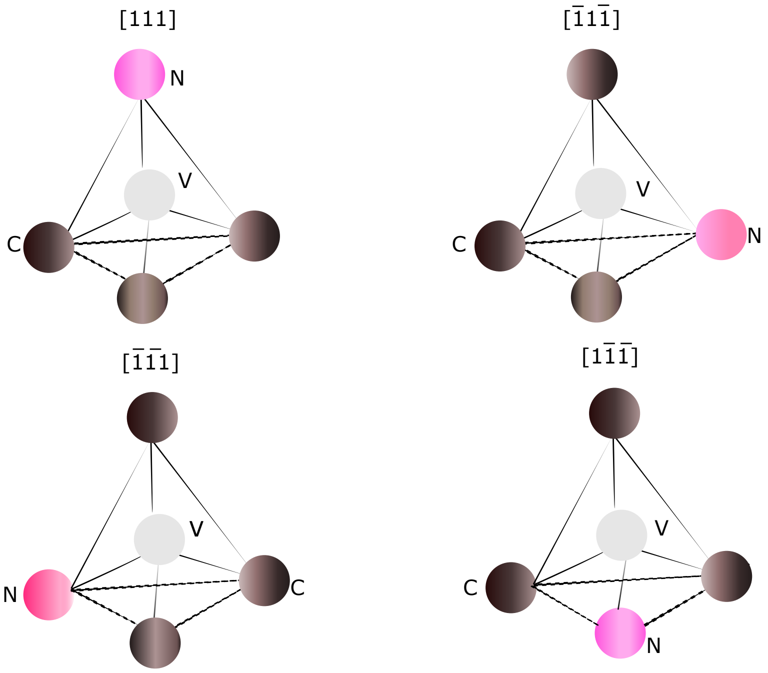

Figure 5.1: Four possible crystallographic orientations of NV center. Image taken and modified from [73]

shown in Fig.5.1 [26]. The center can possess three possible charges such as NV^-, NV^0 and NV^+. NV^0 has five electrons coming from three dangling bond of the carbon atoms and the two lone pair electrons of the Nitrogen atom. The center can gain a charge of positive or negative respectively depending on the presence of acceptors or donors in the lattice. NV^- and NV^0 can be identified by their optical Zero Phonon Lines (ZPL) at 1.945 eV(637nm) and 2.156 eV(575nm) respectively. And, the associated vibronic bands extend the ZPL to higher in absorption and lower in emission [24]. An additional infrared ZPL at 1.190 eV (1042nm) has been observed associated with NV^- center under optical illumination. NV^- and NV^0 have been observed experimentally, but NV^+ is still a theoretical prediction. This thesis mainly focuses on NV^- centers and now onwards I refer NV^- center as NV center.

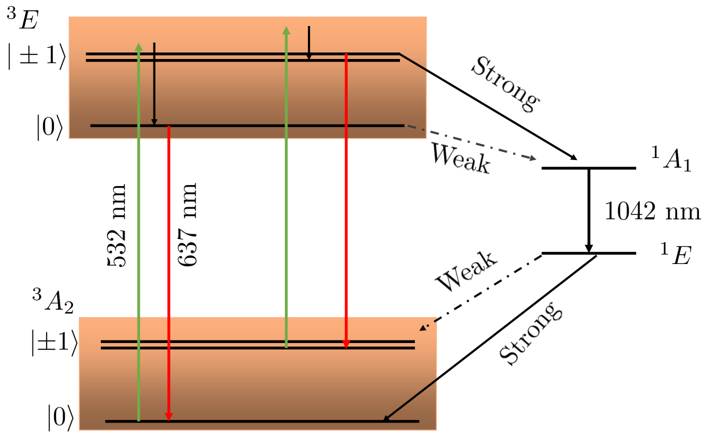

Figure 5.2: NV center can be described by a triplet ground state, a triplet excited state and a singlet intermediate state. NV center is excited with a 532 nm laser and the spin conserving optical transitions are possible between ground and excited state with a zero phonon line of 637 nm.

Electronic Structure of NV Center

NV center possesses six valence electrons, hence it has a electron spin, $S = 1$. From the group theory, NV center has a spin-triplet Ground state with $^3A_2$ symmetry and a spin triplet of ^3E symmetry excited state. And, it also possesses intermediate singlet states described by $^1A_1$ and ^1E. The electronic structure of NV center is shown in Fig.5.2.

Spin Initialization and readout

NV center can be excited from off-resonantly by a 532nm laser. Consequently, a spin preserving transition fluorescence occurs between the $^3A_2$ and the ^3E states. Also, an extra decay path through Inter-System Crossing (ISC) is enabled via the intermediate singlet states and it is a non radiative decay ($ZPL = 1042nm$). And, this plays a major role in the spin initialization and readout of NV center. The state, $m_s = |\pm 1\rangle$ 30% higher probability for undergoing ISC compared to $m_s = |0\rangle$ state. Fluorescence along with ISC optically pump the NV center predominantly into $m_s = |0\rangle$ ground state. The Florescence lifetimes of the excited NV center is of 12 ns for the $m_s = |0\rangle$ state and 7.8 ns for the $m_s = |\pm 1\rangle$ state. However, ISC takes about 300 ns to decay to $m_s = |0\rangle$

state.

The Electronic spin state can be distinguished by the differential fluorescence between $m_s = |0\rangle$ and $m_s = |\pm 1\rangle$ state. The NV center which is initialized into $m_s = |\pm 1\rangle$ state emits about 30% less number of photons than that of $m_s = |0\rangle$ state. Therefore, NV center can be initialized as well as readout via optical pumping. we can distinguish between the two quantum state $m_s = |0\rangle$ and $m_s = |\pm 1\rangle$ state by counting the florescent photons, hence once can realize a qubit by considering these two states.

In NV center experiments, the readout performance is quantified by the signal-to-noise ratio(SNR) and the signal is generally the number of photon detected in a fixed readout cycle [47] . Therefore, SNR can be defined as:

$$SNR = \frac{\alpha_0 - \alpha_1}{\sqrt{\alpha_0 + \alpha_1}} \tag{5.1}$$

where, α_i is the average photon detected for a single measurement of spin state $|i\rangle$. And, contrast between the two signals can be written as:

$$C = (1 - \frac{\alpha_1}{\alpha_0}) \tag{5.2}$$

The contras, $C \approx 0.3$ for an NV center in bulk diamond during the typical fluorescent based readout method. However, we often need to average the signal by repeating the experiments many times to improve the SNR. Therefore, time averaged SNR after N measurements is:

$$< SNR >= \sqrt{N} \times SNR \tag{5.3}$$

NV Center Hamiltonian

In this section, I shall discuss the Ground state Hamiltonian of the NV center. The Hamiltonian mainly has three parts: electronic spin Hamiltonian, nuclear spin Hamiltonian and electron-nuclei spin Hamiltonian which is the hyperfine interaction. Therefore, the general ground state Hamiltonian of the NV center can be written as

$$\mathcal{H}_{gs} = \mathcal{H}_e + \mathcal{H}_n + \mathcal{H}_{hf}. \tag{5.4}$$

Electronic Spin Hamiltonian

The NV center is effectively a two unpaired electronic system with a electronic spin $I = 1$. The ground state electronic spin Hamiltonian consists of two parts namely Zero Field Splitting (ZFS) which occurs due to the crystallographic field and the Zeeman field which is the splitting due to the external magnetic field. Consequently, the electronic spin Hamiltonian in the unit of the Plank's constant,h, can be written as,

$$\mathcal{H}_e = \mathcal{H}_{ZFS} + \mathcal{H}_{zeeman} = \mathcal{D}_{gs}[S_z^2 - E(S_x^2 - S_y^2)] + \gamma_e B_0 S_z. \tag{5.5}$$

where, $\gamma_e = 2.8025 MHz/G$ is the gyro-magnetic ratio of the NV center, $\mathcal{D}_{gs} \approx 2.87 GHz$ is the ground state ZFS component at room temperature, E is the off-axis component of the ZFS ($E << D$) and $S = (S_x, S_y S_z)$ are the spin angular momentum operators of the NV center where,

$$S_x = \frac{h}{\sqrt{2}} \begin{bmatrix} 0 & 1 & 0 \\ 1 & 0 & 1 \\ 0 & 1 & 0 \end{bmatrix} \qquad S_x = \frac{ih}{\sqrt{2}} \begin{bmatrix} 0 & -1 & 0 \\ 1 & 0 & -1 \\ 0 & 1 & 0 \end{bmatrix} \qquad S_x = h \begin{bmatrix} 1 & 0 & 0 \\ 0 & 0 & 0 \\ 0 & 0 & -1 \end{bmatrix}$$

For the simplicity, we assume the external field is aligned along the NV axis which is generally considered as the Z-axis hence the Zeeman Hamiltnian only has the contri-

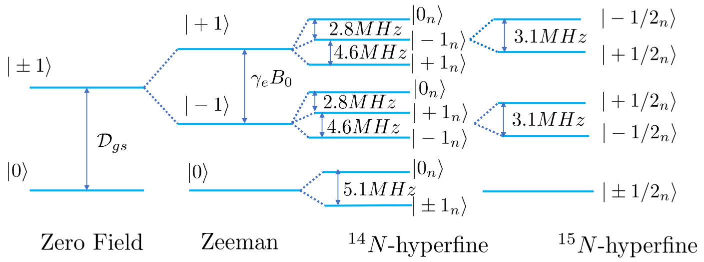

Figure 5.3: NV energy level splittings with different interactions including Zero Field Splitting, Zeeman interaction and hyperfine interaction with ^{14}N or ^{15}N. The nuclear spin eigen states are shown with a subscript 'n'. Image taken and modified from [73]

bution from the S_z component.

Nuclear spin and Electron-Nuclei Hamiltonian

The Nitrogen atom in the NV center has a nuclear spin, I. The Nitrogen has two possible Isotops such as ^{14}N with $I = 1$ and ^{15}N with $I = 1/2$. The natural abundant of ^{14}N isotop is 99.6%. Depending on the isotops of Nitrogen atom, the Nuclear part can have upto two parts:- nuclear Zeeman splitting which shifts the nuclear eigen states and the quadrapolar part which is only present in the case of $I > 1/2$. Besides, NV center can be often surrounded by one or more ^{13}C carbon atoms of spin $I = 1/2$. The nuclear spin Hamiltonian can be described as;

$$\mathcal{H}_n = \mathcal{H}_{Zeeman(n)} + \mathcal{H}_Q = -\sum_{i=1}^{N}(\gamma_i B_0.I) + Q(I_z^2 - \frac{1}{3}I(I+1)). \tag{5.6}$$

The Hamiltonian parameters are listed in Table.5.1.

The next part of the Hamiltonian is due to the interaction between NV center and the nuclear spin and it is known as the hyperfine interaction. The hyperfine Hamiltonian can be written as,

$$\mathcal{H}_{hf} = \sum_{i=1}^{N} SA_iI_i = \sum_{i=1}^{N} A_i^{\|} S_z I_{zi} + A_i^{\perp}(S_x I_{xi} + S_y I_{yi}) \tag{5.7}$$

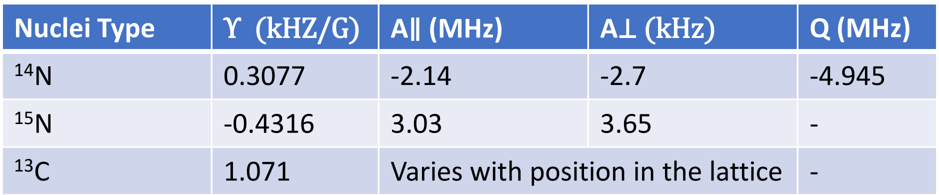

Nuclei Type	ϒ (kHZ/G)	A∥ (MHz)	A⊥ (kHz)	Q (MHz)
^{14}N	0.3077	-2.14	-2.7	-4.945
^{15}N	-0.4316	3.03	3.65	-
^{13}C	1.071	Varies with position in the lattice		-

Table 5.1: Hamiltonian parameters corresponding to different nuclei coupled to the NV center. The values are taken from [31, 32]

where, A_i is the hyperfine tensor and it can be diagonalized to have the form:

$$A = \begin{bmatrix} A^{\perp} & 0 & 0 \\ 0 & A^{\perp} & 0 \\ 0 & 0 & A^{\parallel} \end{bmatrix}$$

where $A^{\parallel}$ and $A^{\perp}$ are the parallel and perpendicular components of the A tensor respectively. Again, the hyperfine interaction parameters corresponding to different nuclei are shown in Table.5.1 and the energy level splittings due to different interactions are depicted in Fig.5.3. However, the hyperfine tensor can be varied for the $^{1}3C$ nuclei depending on the position of the carbon atom in the diamond lattice.

Chapter 6

Experimental Setup

In this chapter, I shall discuss the confocal setup for addressing the defect centers in diamond and the microwave setup for the spin manipulations of those centers. And, I will also discuss some of the experimental results.

Confocal Microscope

Confocal microscope is used for selective imaging of different points in the source plane by blocking the lights from all other points in the source plane [12]. This can be accomplished by placing a pinhole in the image plane such that only the light from the point of interest is passed through the pinhole. Although a confocal microscope can be built using two biconvex lenses and a pinhole, in practice, it can be more complex and requiring more optical components. A schematic of the simplest confocal setup is shown in Fig.6.1

A scanning confocal enables the access of more than one point in the source plane [66, 69]. It can be achieved either by sweeping the pinhole position in the image plane or by moving the source plane such that the lights from the new source point of interest is collected by the pinhole. In our case, we used the later method that is moving the source plane for obtaining the scanning image of the diamond hence finding out the NV

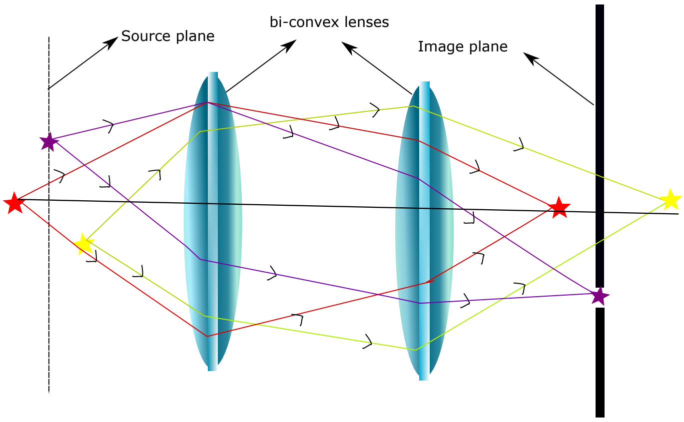

Figure 6.1: A simple confocal setup. The conjugate nature of source plane and image plane is shown by considering three points in the source plane at different depths focusing at the image plane after passing through two biconvex lenses.The pinhole blocks the lights from the other points except the light from the point source of interest. Image adopted and modified from [79]

centers.

Scanning, Fluorescent Confocal Microscope

A scanning confocal microscope was built using various optical components as shown in Fig.6.2. In this section, I will be explaining the confocal setup in detail.

The most important part of the florescent confocal technique is to excite the NV center with the right wavelength laser and in our case it is 532 nm. Ideally, a laser with spatial mode TEM_{00} is preferred. We used 1 W Gem-532 laser from Laser Quantum GmbH. Although, the NV centers were never excited with a power more than 150 mW during our experiments and the power is controlled using the remote laser control software provided by the same company .

Often during NV experiments, the laser needs to be turned on and turned off in a highly controlled manner. This is done by using an Acousto-Optic Modulator(AOM). We used a AOM of crystalline quartz optical medium with an acoustic velocity of 5.74 $mm/\mu s$ from Gooch $\&$ Housego. The refractive index of the optical medium can be changed by introducing mechanical oscillations in the medium. A piezoelectric material

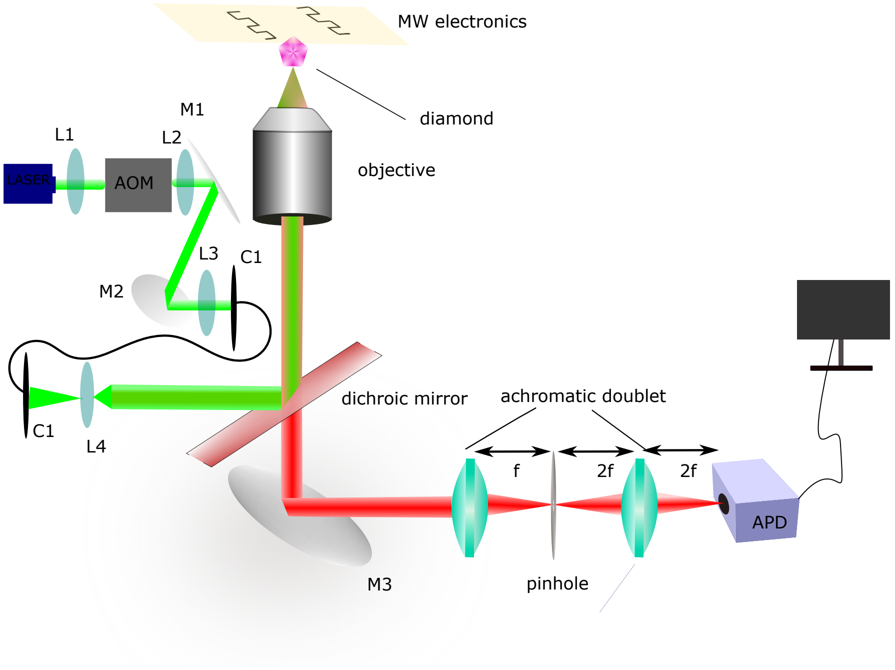

Figure 6.2: Fluorescent confocal setup.

which is attached to the optical medium is driven by a RF signal to produce mechanical oscillations in the piezoelectric material thereby creating oscillations in the optical medium. The compression and rarefaction in the material introduce regions of low and high refractive indices and it will act like a diffraction grating. The first order diffraction beam is picked off with an iris and blocked all other orders. The maximum first order efficiency ($> 98\%$) is achieved with a RF driver of frequency 250 MHz and RF power 6.6 W. The RF driver of rising time 20 ns is controlled using the TTL input which is generator by the pulseblaster (SpinCore PBESR-PRO-500).

The AOM is placed at the focal point of the L_1 (LA1608-A, Thorlabs). This is to ensure that the beam size is smaller than the active area of the AO medium which is 0.25 mm $\times$ 0.25 mm. The original beam diameter of our laser is ≈ 1 m. The first order is again a diverging beam and we placed a lens L2 (LA1484-A, Thorlabs) at the focal plane from the AOM output to make it collimated.

It is assumed that the first diffraction order is not completely Gaussian and the Gaussian mode is filtered using a single mode fiber (P1-460B-FC-2, Thorlabs). The maximum fiber coupling efficiency is achieved only if the incident laser is highly collimated. The fiber coupler, c1 (SM1FC-FC/PC, Thorlabs) is placed at the focal point of an achromatic lens L3 (AC050-015-A-ML, Thorlabs) which was mounted on a xyz stage(XYZCTS50, Holmarc Pvt. Ltd). The other end of the fiber acts as a point source hence the light coming out of the fiber is diverging. Therefore, the fiber end is placed at the focus of a small focal length lens, L4 (LA1951-A, Thorlabs), so that the laser beam is again collimated. The telescope which consist of mirrors M1 (BB1-E02-10, Thorlabs) and M2 (BB1-E02-10, Thorlabs) gives the additional degrees of freedom. We found that the beam expansion after the L4 was sufficient enough to completely fill the back plane of the objective thereby achieving the tight focusing. So we didn't have to expand the beam further.

Next, a dichroic mirror (DMLP567R, Thorlabs) is placed before the objective which has high reflectivity for the green light and high transmittivity in the red region. Therefore, the red fluorescent from the NV which is collected at the detector. A 100X magnification, oil immersion objective with a numerical aperture 1.4 from Olympus (UPLSAPO 100XO) is used in our setup. The objective was placed on a PI nano-stage (P-527.2CL) with a closed loop travel of 200 μm in both x and y axes and 50 μm in the z axis.

The diamond sample is glued on a home designed PCB board and it is mounted on a xyz micro stage. The 3D translational stage was constructed by combing a xy stage (XYT1/M, Thorlabs) unit and a z stage unit (MVS010/M, Thorlabs) along with an extended top platform (AMA005/M, Thorlabs). The light emitted from the sample which is in the wavelength range 600-800 nm transmits through the dichroic mirror and focused it to a pinhole using an achromatic lens with focal length f=100 mm (ACN254-

Figures/ConfocalImageNVs.jpg

Figure 6.3: Confocal Image. The diffraction limited red spots are the high Fluorescent regions and those are the locations of NV centers in the diamond sample.

100-A, Thorlabs) which is mounted on a xyz (XYZCT65, Holmarc Pvt. Ltd) stage for the fine adjustments. Another achromatic lens with with focal length of 50 mm (ACN254-50-A, Throlabs) is placed at a distance 2f from the 50 μm pinhole (P50D, Thorlabs) and the light is collected by a single photon counting module (SPCM-AQRH-W4, Excelitas) with a dark count of 100 c/s. The data acquisition from the SPCMS done using a NI DAQ card from National Instruments (NIPCIe 6363) and a scanning counter software is developed using LABVIEW. A 10 $\mu m \times 10$ μm xy scanning image obtained is shown in Fig.6.3. This image is obtained by performing a scanning on a sample where there are many single color centers and all other pulsed experiments (will be discussed at the end of this chapter) are done on a different sample with ensemble NV center.

Microwave Circuit

A basic microwave circuit was built for manipulating the electronic spins of the NV center. A copper wire strapped across the diamond sample delivers the microwaves to the sample. Both ends of the copper wire is soldered tightly on the PCB sample holder.

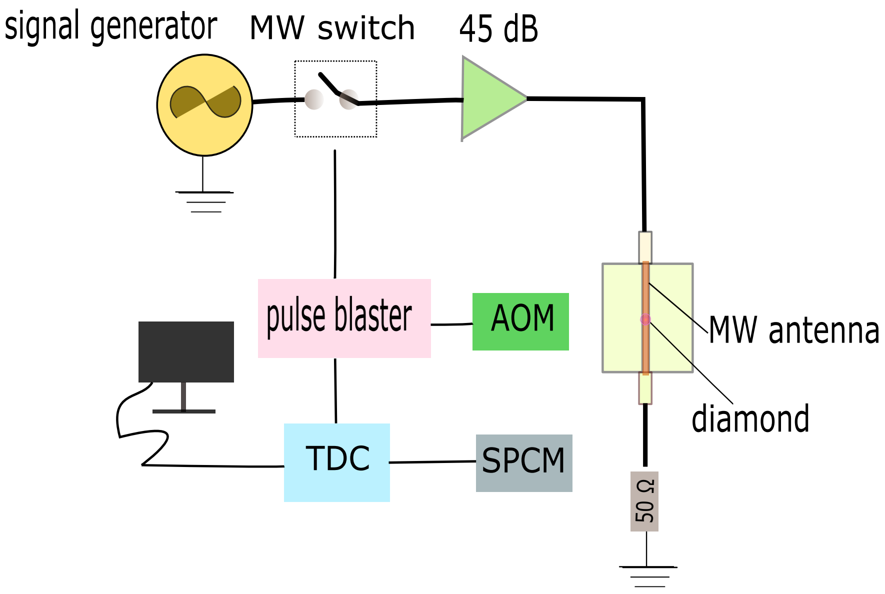

Figure 6.4: Microwave Circuit.

A microwave generated by the Keysight N9310A microwave generator is amplified up to 16 W after the amplifier (ZHL-16W-43+, Mini-Circuits) is passed through copper wire. A microwave switch (ZYSW-2-50DR, Mini-Circuits) is placed before the amplifier for turning it on while it is needed. The microwave switch is trigged with the TTL pulses generated by the same Pulseblaster which is used for triggering the AOM controller. The same pulseblaster is also used for triggering the fast counting device (FAST ComTec MCS6A) whcih recorded the photon counting events from the SPCM during pulsed experiments. In addition to it, the microwave switch is used to achieve the desired microwave pulse duration. The outcoming microwave after the PCB board is attenuated using a MW attenuator (VAT-2W2+, Mini-Circuits) and finally terminated using a 50 Ω terminator (KARN-50+, Mini-Circuits). The schematic of the microwave circuit is shown in Fig.6.4. The current microwave circuit is incapable of controlling the phases of the microwave and this can be achieved by introducing an additional arbitrary wave generator (AWG) and a IQ mixer. This will part will be looked up in the future.

Experiments

The main three stages of NV center experiments are spin initialization, spin manipulations and Readout of the final spin state. Both spin initialization and readout are done optically applying laser pulses of duration 2 μs.The confocal setup addresses the fluorescing defects centers in diamond and it is not alone sufficient to confirm if it is a NV center or not. Therefore, we performed the Optically Detected Magnetic Resonance (ODMR) for confirming those are NV center.

Continuous Wave ODMR

The electronic structure of the NV center can be characterized by applying microwave of different frequency to the diamond sample. In continuous wave ODMR, the NV centers are initialized into $m_s = 0$ spin state by applying a laser pulse of duration 2 μs. When the microwave frequency matches the energy level between $m_s = \pm 1$, the spin state of the NV center is rotated between the energy level, hence there will be a drop in the fluorescent count. The florescent response during laser pulse while the NV center is initialized into different spin states are shown in Fig.6.5 [44]. In the presence of an external magnetic field, the degeneracy between $m_s = \pm 1$ is lifted and consequently we observe two resonant frequencies. The ODMR spectra we observed are shown in Fig6.6.

Rabi Flops Experiments

We confirmed NV centers by performing ODMR and the next step was to characterize the coherent properties of them. We performed the basics pulsed experiments such as Rabi, Ramsey Oscillations and spin relaxation experiments.During pulsed experiments,the fast counter recorded the events at the SPCM of the whole measurement sequence.

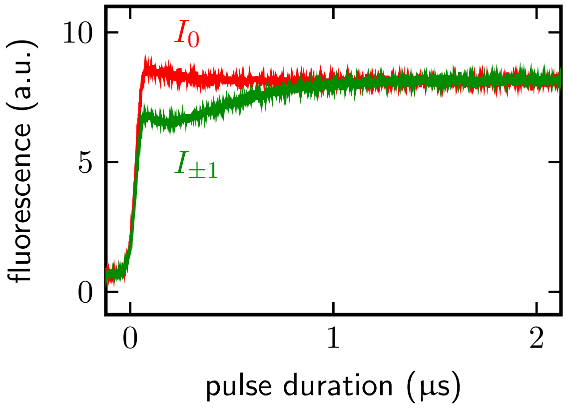

Figure 6.5: Flourescence response during laser pulse while NV center is initialized in $m_s = 0$ (Red) and $m_s = \pm 1$ (green). Image modified from the referece [73]

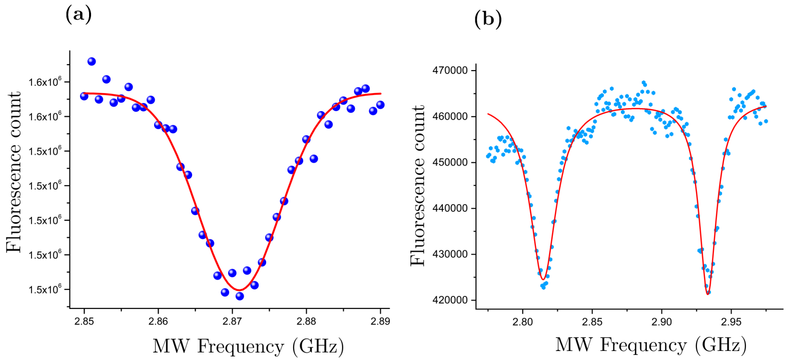

Figure 6.6: Zero Field splitting (ZFS) ODMR.(a) The fluorescence response was dropped at the frequency $\nu = 2.87$ GHz which corresponding to the ZFS between $m_s = 0$ and $m_s = \pm 1$. (b) ODMR performed with an external field aligned along one out of 4 possible orientations and the spitting between the $|-1\rangle$ and $|+1\rangle$ transitions is given by $\Delta\nu = 2\gamma_{NV} B_z$ where γ_{NV} is the gyromagnetic ratio of the NV center and B_z is the magnetic field along the NV axis. Other 3 possible orientations are symmetric to the aligned axis and the splitting due to the component of the B_z along those axes are not resolved due to the high FWHM of the ODMR dips.

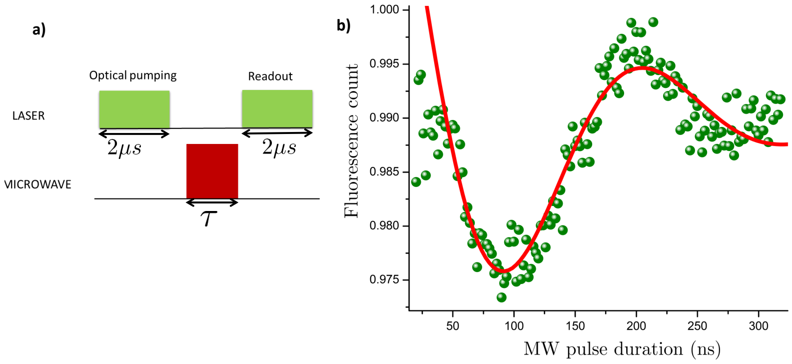

Figure 6.7: Rabi Oscillations. (a) pulse sequence for Rabi experiments. (b) Fluorescent oscillations with the mw pulse duration and the π pulse duration corresponding to the maximum population inversion is $\approx$ 86 ns.

In Rabi flop experiments, strong mw pulses of variable duration are applied. The NV centers are initialized into $m_s = 0$ state. The mw pulses rotate the spin state and bring them into a superposition;

$$\psi = \alpha|0\rangle + \beta|\pm 1\rangle$$

where, $\alpha^2 + \beta^2 = 1$ and the probability amplitudes, α and β vary as a function of mw duration. Consequently, we observe an oscillating fluorescence response as a function of mw pulse duration as shown in Fig. 6.7 [50]. The decay in oscillation gives the information about the spin-spin relaxation time T_2* of the NV center and as we performed experiments on the ensemble NV centers,the T_2* is rather small thus the oscillation decayed faster. in this case,the Rabi nutation frequency, $\Omega = \gamma B_1$ where $\gamma = 2.8$ MHz/ Gauss is the gyro magnetic ratio of the NV center electronic spin and the B_1 is the component of mw excitation field along the NV axis, is found to be 6.28 MHz.

Spin relaxation experiments

The NV center which is initialized into one of the electronic state or the coherent superposition of electronic states often interacts with the environment decays back to the

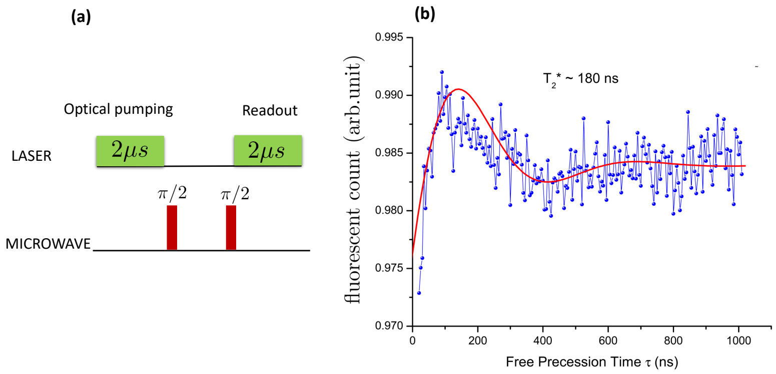

Figure 6.8: Free Induction Decay (FID) curve (a) pulse sequence for characterizing T_2^*. (b) Fluorescent count with the free precession time; the T_2^* is $\approx 180ns$.

thermally mixed states via relaxation processes. These are mainly due to the spin-spin interactions in the ensemble NV centers as well as the other spin impurities such as C^{13} and Nitrogen associated to the NV center. These interactions mainly cause a dephasing in the coherent NV spin sate and it is characterized by the T_2^* [51].

In T_2^* characterization experiments, the NV center is optically initialized into $m_s = 0$ state. Then a $\pi/2$ pulse is applied to create the coherent superposition of two possible electronic spin states and it is written as;

$$\psi_{ini} = (|0\rangle + |\pm 1\rangle)/\sqrt(2) \tag{6.1}$$

Then allow them to freely evolve under its internal Hamiltonian for time τ. During this time, the state ψ_{ini} accumulates a relative phase between $|0\rangle$ and $|\pm 1\rangle)$ due to decoherence. After a time τ, another $\pi/2$ pulse is applied to bring it back to the $|0\rangle$ and $|\pm 1\rangle$ basis. The fluorescent response is recorded as a function of τ and T_2^* is estimated from the decay time. The decaying fluorescent response versus precession time, τ is shown in Fig. 6.8. The oscillations observed in the experiment is due to the offset in the ODMR frequency [18].

The other possible spin relaxation is due to the spin-flips caused by the phononic

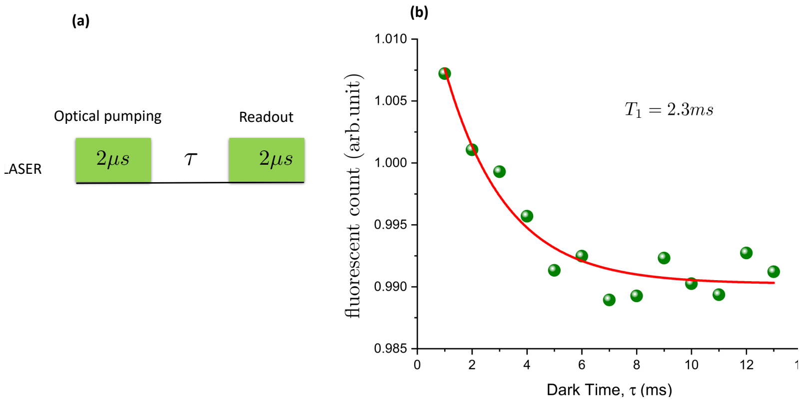

Figure 6.9: T_1 relaxation experiments.

interaction with the crystal lattice and it is characterized by the T_1 time. As a result of this, the spin state initialized into $m_s = 0$ states goes back to the thermal state. This experiments can be performed easily by letting the NV spin which is optically initialized evolve freely for a time τ which we referred as the dark time as it redistribute the populations of the spin states as and the pulse sequence is shown in Fig. 6.9 (a). The decaying fluorescent response as a function of τ is shown in Fig.6.9 (b). The decay time gives the value of T_1 [49, 64] .

Chapter 7

Conclusion and Outlook

Conclusion

In this thesis we successfully showed experimental realization of the recent quantum phenomena called the quantum pigeonhole effect and the implementation of optimal fixed quantum search algorithm. The another main focus of the thesis is to achieve robust quantum control. In some of the experiments, we adapted the popular optimal control technique, GRAPE for realizing optimal control pulses.

We also proposed a novel method for realizing robust controls through bang-bang control. In this technique, the smooth modulation of the control parameters are avoided. Therefore, repeated calculation of basic unitaries during the discrete time steps are not often required hence it is computationally inexpensive. In practice, smooth modulation of RF field is more difficult than turning on and off the full power RF field in a controlled manner. So, here we used the intermittent burst of full power RF field which we called a bang along with free evolution under the intrinsic Hamiltonian of the quantum system.

The another important achievement of this thesis was realizing optimized protected quantum gates by integrating dynamical decoupling and optimal control techniques. In this work, we also look into how to protect non-classical correlations in particular quantum discord during Grover's search algorithm. Quantum correlations are known to be an important resource for quantum computing as well as quantum simulations hence it is important to preserve them during computations. Protected quantum gates happened to show a good advantage in protecting quantum discord over unprotected quantum gates. We also found that a XY-DD with $90°$ pulse angle over performs the $180°$ pulses.

Later during my PhD, we worked on setting up the experimental platform where we can perform quantum information processing using Nitrogen vacancy centers in diamond in the future. Nitrogen vacancy center were gaining great attention for applications in developing quantum technologies such as quantum computer, quantum sensors and metrology. We could successfully build a confocal setup in our lab and address single NV centers in a diamond sample which was lent to us by Dr. Phani Kumar. However, all other spin manipulation experiments were performed on NV ensemble in a bulk diamond which we bought from Diamond Elements Pvt. Ltd. We also, performed spin relaxation studies on NV center ensemble.

Outlook

There are lot of space for improving the techniques and experiments we discussed in this thesis. It would be interesting to address mutually interacting NV center qubits and repeating experiments such as quantum pigeon hole effect and optimal quantum search algorithm on them. It is also possible to apply the optimal control techniques such as GRAPE, BB and optimized protected quantum gates on NV center quantum simulator. In order to implement these technique, we need to incorporate some more electronics such as an extra arbitary wave generator and an IQ mixer in our existing microwave circuit for controlling the phase of the microwave pulses.

Bibliography

[1] Yakir Aharonov and Eliahu Cohen. Weak values and quantum nonlocality. *arXiv preprint arXiv:1504.03797*, 2015.

[2] Yakir Aharonov, Fabrizio Colombo, S Popescu, Irene Sabadini, Daniele C Struppa, and Jeff Tollaksen. The quantum pigeonhole principle and the nature of quantum correlations. *arXiv preprint arXiv:1407.3194*, 2014.

[3] Ashok Ajoy, Gonzalo A Álvarez, and Dieter Suter. Optimal pulse spacing for dynamical decoupling in the presence of a purely dephasing spin bath. *Phys. Rev. A*, 83(3):032303, 2011.

[4] Miklós Ajtai. The complexity of the pigeonhole principle. In *Foundations of Computer Science, 1988., 29th Annual Symposium on*, pages 346–355. IEEE, 1988.

[5] Gonzalo A Alvarez, Ashok Ajoy, Xinhua Peng, and Dieter Suter. Performance comparison of dynamical decoupling sequences for a qubit in a rapidly fluctuating spin bath. *Phys. Rev. A*, 82(4):042306, 2010.

[6] MS Anwar, L Xiao, AJ Short, JA Jones, D Blazina, SB Duckett, and HA Carteret. Practical implementations of twirl operations. *Physical Review A*, 71(3):032327, 2005.

[7] Charles H Bennett, Gilles Brassard, Seth Breidbart, and Stephen Wiesner. Quantum cryptography, or unforgeable subway tokens. In *Advances in Cryptology*, pages 267–275. Springer, 1983.

[8] Charles H Bennett and David P DiVincenzo. Quantum information and computation. *Nature*, 404(6775):247, 2000.

[9] Gaurav Bhole, V. S. Anjusha, and T. S. Mahesh. Steering quantum dynamics via bang-bang control: Implementing optimal fixed-point quantum search algorithm. *Phys. Rev. A*, 93:042339, Apr 2016.

[10] Gaurav Bhole and T. S. Mahesh. Rapid exponentiation using discrete operators: Applications in optimizing quantum controls and simulating quantum dynamics. *arXiv preprint arXiv:1707.02162*, 2017.

[11] Geoffrey Bodenhausen, Ray Freeman, and Gareth A Morris. A simple pulse sequence for selective excitation in fourier transform nmr. *Journal of Magnetic Resonance (1969)*, 23(1):171–175, 1976.

[12] Max Born and Emil Wolf. *Principles of optics: electromagnetic theory of propagation, interference and diffraction of light*. Elsevier, 2013.

[13] Richard A Brualdi. *Introductory combinatorics*. New York, 1992.

[14] FP Bundy, H Tracy Hall, HM Strong, and RH Wentorf Jun. Man-made diamonds. *nature*, 176(4471):51, 1955.

[15] Samuel R Buss. Polynomial size proofs of the propositional pigeonhole principle. *The Journal of Symbolic Logic*, 52(04):916–927, 1987.

[16] JE Butler, Yu A Mankelevich, A Cheesman, Jie Ma, and MNR Ashfold. Understanding the chemical vapor deposition of diamond: recent progress. *Journal of Physics: Condensed Matter*, 21(36):364201, 2009.

[17] John Cavanagh. *Protein NMR spectroscopy: principles and practice*. Academic Pr, 1996.

[18] L Childress, MV Gurudev Dutt, JM Taylor, AS Zibrov, F Jelezko, J Wrachtrup, PR Hemmer, and MD Lukin. Coherent dynamics of coupled electron and nuclear spin qubits in diamond. *Science*, 314(5797):281–285, 2006.

[19] Lilian Childress and Ronald Hanson. Diamond nv centers for quantum computing and quantum networks. *MRS bulletin*, 38(2):134–138, 2013.

[20] J Ignacio Cirac and Peter Zoller. Goals and opportunities in quantum simulation. *Nature Physics*, 8(4):264, 2012.

[21] David G Cory, Amr F Fahmy, and Timothy F Havel. Ensemble quantum computing by nmr spectroscopy. *Proceedings of the National Academy of Sciences*, 94(5):1634–1639, 1997.

[22] David G Cory, Mark D Price, and Timothy F Havel. Nuclear magnetic resonance spectroscopy: An experimentally accessible paradigm for quantum computing. *Physica D: Nonlinear Phenomena*, 120(1):82–101, 1998.

[23] Animesh Datta, Anil Shaji, and Carlton M Caves. Quantum discord and the power of one qubit. *Phys. Rev. Lett.*, 100(5):050502, 2008.

[24] Gordon Davies. The a nitrogen aggregate in diamond-its symmetry and possible structure. *Journal of Physics C: Solid State Physics*, 9(19):L537, 1976.

[25] David P DiVincenzo and Daniel Loss. Quantum information is physical. *Superlattices and Microstructures*, 23(3-4):419–432, 1998.

[26] Marcus W Doherty, Neil B Manson, Paul Delaney, Fedor Jelezko, Jörg Wrachtrup, and Lloyd CL Hollenberg. The nitrogen-vacancy colour centre in diamond. *Physics Reports*, 528(1):1–45, 2013.

[27] MV Gurudev Dutt, L Childress, L Jiang, E Togan, J Maze, F Jelezko, AS Zibrov, PR Hemmer, and MD Lukin. Quantum register based on individual electronic and nuclear spin qubits in diamond. *Science*, 316(5829):1312–1316, 2007.

[28] Artur K Ekert. Quantum cryptography based on bells theorem. *Physical review letters*, 67(6):661, 1991.

[29] Michael Edward Factor and Eitan Daniel Farchi. Caching in a data processing system using the pigeon hole principle. July 25 2000. US Patent 6,094,706.

[30] Felipe Fernandes Fanchini, Diogo de Oliveira Soares Pinto, and Gerardo Adesso. *Lectures on General Quantum Correlations and Their Applications*. Springer, 2017.

[31] S Felton, AM Edmonds, ME Newton, PM Martineau, D Fisher, DJ Twitchen, and JM Baker. Hyperfine interaction in the ground state of the negatively charged nitrogen vacancy center in diamond. *Physical Review B*, 79(7):075203, 2009.

[32] Solveig Felton, AM Edmonds, Mark E Newton, PM Martineau, D Fisher, and DJ Twitchen. Electron paramagnetic resonance studies of the neutral nitrogen vacancy in diamond. *Physical Review B*, 77(8):081201, 2008.

[33] Richard P Feynman. Simulating physics with computers. *International journal of theoretical physics*, 21(6):467–488, 1982.

[34] Evan M Fortunato, Marco A Pravia, Nicolas Boulant, Grum Teklemariam, Timothy F Havel, and David G Cory. Design of strongly modulating pulses to implement precise effective hamiltonians for quantum information processing. *The Journal of chemical physics*, 116(17):7599–7606, 2002.

[35] Ray. Freeman. Selective excitation in high-resolution nmr. *Chemical Reviews*, 91(7):1397–1412, 1991.

[36] Ray Freeman and Wu Xili. Design of magnetic resonance experiments by genetic evolution. *Journal of Magnetic Resonance (1969)*, 75(1):184–189, 1987.

[37] BM Fung. Pairs of pseudopure states for 4-and 5-qubit nuclear magnetic resonance systems. *The Journal of Chemical Physics*, 115(17):8044–8048, 2001.

[38] Neil A Gershenfeld and Isaac L Chuang. Bulk spin-resonance quantum computation. *science*, 275(5298):350–356, 1997.

[39] BC Gerstein. High-resolution nmr in solids with strong homonuclear dipolar broadening: combined multiple-pulse decoupling and magic angle spinning. *Phil. Trans. R. Soc. Lond. A*, 299(1452):521–546, 1981.

[40] Lov K Grover. A fast quantum mechanical algorithm for database search. *arXiv preprint quant-ph/9605043*, 1996.

[41] Lov K Grover. Quantum mechanics helps in searching for a needle in a haystack. *Physical review letters*, 79(2):325, 1997.

[42] Lov K Grover. Quantum mechanics helps in searching for a needle in a haystack. *Physical review letters*, 79(2):325, 1997.

[43] Lov K Grover. Fixed-point quantum search. *Physical Review Letters*, 95(15):150501, 2005.

[44] A Gruber, A Dräbenstedt, C Tietz, L Fleury, J Wrachtrup, and C Von Borczyskowski. Scanning confocal optical microscopy and magnetic resonance on single defect centers. *Science*, 276(5321):2012–2014, 1997.

[45] Ulrich Haeberlen. *High Resolution NMR in solids selective averaging: supplement 1 advances in magnetic resonance*, volume 1. Elsevier, 2012.

[46] Michael K Henry, Alexey V Gorshkov, Yaakov S Weinstein, Paola Cappellaro, Joseph Emerson, Nicolas Boulant, Jonathan S Hodges, Chandrasekhar Ramanathan, Timothy F Havel, Rudy Martinez, et al. Signatures of incoherence in a quantum information processor. *Quantum Information Processing*, 6(6):431–444, 2007.

[47] David Hopper, Henry Shulevitz, and Lee Bassett. Spin readout techniques of the nitrogen-vacancy center in diamond. *Micromachines*, 9(9):437, 2018.

[48] Ryszard Horodecki, Pawel Horodecki, Michal Horodecki, and Karol Horodecki. Quantum entanglement. *Reviews of modern physics*, 81(2):865, 2009.

[49] A Jarmola, VM Acosta, K Jensen, S Chemerisov, and D Budker. Temperature- and magnetic-field-dependent longitudinal spin relaxation in nitrogen-vacancy ensembles in diamond. *Physical review letters*, 108(19):197601, 2012.

[50] Fedor Jelezko, T Gaebel, I Popa, A Gruber, and Jorg Wrachtrup. Observation of coherent oscillations in a single electron spin. *Physical review letters*, 92(7):076401, 2004.

[51] Liang Jiang, JS Hodges, JR Maze, Peter Maurer, JM Taylor, DG Cory, PR Hemmer, Ronald Lee Walsworth, Amir Yacoby, Alexander S Zibrov, et al. Repetitive

readout of a single electronic spin via quantum logic with nuclear spin ancillae. *Science*, 326(5950):267–272, 2009.

[52] Hemant Katiyar, Soumya Singha Roy, T. S. Mahesh, and Apoorva Patel. Evolution of quantum discord and its stability in two-qubit nmr systems. *Physical Review A*, 86(1):012309, 2012.

[53] Navin Khaneja, Timo Reiss, Cindie Kehlet, Thomas Schulte-Herbrüggen, and Steffen J Glaser. Optimal control of coupled spin dynamics: design of nmr pulse sequences by gradient ascent algorithms. *Journal of Magnetic Resonance*, 172(2):296–305, 2005.

[54] Navin Khaneja *et. al.* Optimal control of coupled spin dynamics: design of nmr pulse sequences by gradient ascent algorithms. *Journal of Magnetic Resonance*, 172(2):296, 2005.

[55] Kaveh Khodjasteh and Lorenza Viola. Dynamically error-corrected gates for universal quantum computation. *Phys. Rev. Lett.*, 102(8):080501, 2009.

[56] Malcolm H Levitt. *Spin dynamics: basics of nuclear magnetic resonance*. John Wiley & Sons, 2001.

[57] Malcolm H Levitt. *Spin dynamics: basics of nuclear magnetic resonance*. John Wiley & Sons, 2001.

[58] Daniel A Lidar. Review of decoherence free subspaces, noiseless subsystems, and dynamical decoupling. *arXiv preprint arXiv:1208.5791*, 2012.

[59] Seth Lloyd. Universal quantum simulators. *Science*, pages 1073–1078, 1996.

[60] Xiao-Ming Lu, Jian Ma, Zhengjun Xi, and Xiaoguang Wang. Optimal measurements to access classical correlations of two-qubit states. *Phys. Rev. A*, 83:012327, Jan 2011.

[61] T. S. Mahesh, C. S. Sudheer Kumar, and Udaysinh T. Bhosale. Quantum correlations in nmr systems. pages 499–516, 2017.

[62] TS Mahesh and Dieter Suter. Quantum-information processing using strongly dipolar coupled nuclear spins. *Physical Review A*, 74(6):062312, 2006.

[63] Peter Mansfield. Snapshot magnetic resonance imaging (nobel lecture). *Angewandte Chemie International Edition*, 43(41):5456–5464, 2004.

[64] NB Manson, JP Harrison, and MJ Sellars. Nitrogen-vacancy center in diamond: Model of the electronic structure and associated dynamics. *Physical Review B*, 74(10):104303, 2006.

[65] VS Manu and Anil Kumar. Singlet-state creation and universal quantum computation in nmr using a genetic algorithm. *Physical Review A*, 86(2):022324, 2012.

[66] Minsky Marvin. Microscopy apparatus, December 19 1961. US Patent 3,013,467.

[67] Ivan I Maximov, Zdeněk Tošner, and Niels Chr Nielsen. Optimal control design of nmr and dynamic nuclear polarization experiments using monotonically convergent algorithms. *The Journal of Chemical Physics*, 128(18):05B609, 2008.

[68] Eric C Milner and Richard Rado. The pigeon-hole principle for ordinal numbers. *Proceedings of the London Mathematical Society*, 3(1):750–768, 1965.

[69] Marvin Minsky. Memoir on inventing the confocal scanning microscope. *Scanning*, 10(4):128–138, 1988.

[70] Avik Mitra, K Sivapriya, and Anil Kumar. Experimental implementation of a three qubit quantum game with corrupt source using nuclear magnetic resonance quantum information processor. *Journal of Magnetic Resonance*, 187(2):306–313, 2007.

[71] Gareth A Morris and Ray Freeman. Selective excitation in fourier transform nuclear magnetic resonance. *Journal of Magnetic Resonance (1969)*, 29(3):433–462, 1978.

[72] John JL Morton, Alexei M Tyryshkin, Arzhang Ardavan, Simon C Benjamin, Kyriakos Porfyrakis, SA Lyon, and G Andrew D Briggs. Bang–bang control of fullerene qubits using ultrafast phase gates. *Nature Physics*, 2(1):40–43, 2006.

[73] Christoph Müller. *Sensing single spins with colour centres in diamond.* PhD thesis, Universität Ulm, 2016.

[74] Michael A Nielsen and Isaac L Chuang. *Quantum computation and quantum information*. Cambridge university press, 2010.

[75] MA Nielson and IL Chuang. *Quantum computation and quantum information (Cambridge Series on Information and the Natural Sciences)[Paperback]*. Cambridge, 2000.

[76] Harold Ollivier and Wojciech H. Zurek. Quantum discord: A measure of the quantumness of correlations. *Phys. Rev. Lett.*, 88:017901, Dec 2001.

[77] H Pape, L Riepe, JR Schopper, et al. A pigeon-hole model for relating permeability to specific surface. *The Log Analyst*, 23(01), 1982.

[78] Jeff B Paris, Alex J Wilkie, and Alan R. Woods. Provability of the pigeonhole principle and the existence of infinitely many primes. *The Journal of Symbolic Logic*, 53(04):1235–1244, 1988.

[79] Om Patange. On an instrument for the coherent investigation of nitrogen-vacancy centres in diamond. Master's thesis, University of Waterloo, 2013.

[80] Xinhua Peng, Dieter Suter, and Daniel A Lidar. High fidelity quantum memory via dynamical decoupling: theory and experiment. *Journal of Physics B: Atomic, Molecular and Optical Physics*, 44(15):154003, 2011.

[81] Alastair Rae and Ted Forgan. On the implications of the quantum-pigeonhole effect. *arXiv preprint arXiv:1412.1333*, 2014.

[82] Robert Raussendorf and Hans J Briegel. A one-way quantum computer. *Phys. Rev. Lett.*, 86(22):5188, 2001.

[83] Xing Rong, Jianpei Geng, Zixiang Wang, Qi Zhang, Chenyong Ju, Fazhan Shi, Chang-Kui Duan, and Jiangfeng Du. Implementation of dynamically corrected gates on a single electron spin in diamond. *Phys. Rev. Lett.*, 112:050503, Feb 2014.

[84] SS Roy and TS Mahesh. Density matrix tomography of singlet states. *Journal of magnetic resonance (San Diego, Calif.: 1997)*, 206(1):127–133, 2010.

[85] Min Ru. *Nevanlinna theory and its relation to Diophantine approximation*. World Scientific, 2001.

[86] JH Shim, I Niemeyer, J Zhang, and D Suter. Robust dynamical decoupling for arbitrary quantum states of a single nv center in diamond. *EPL (Europhysics Letters)*, 99(4):40004, 2012.

[87] Peter W Shor. Scheme for reducing decoherence in quantum computer memory. *Physical review A*, 52(4):R2493, 1995.

[88] Peter W Shor. Polynomial-time algorithms for prime factorization and discrete logarithms on a quantum computer. *SIAM review*, 41(2):303–332, 1999.

[89] Abhishek Shukla. Ancilla assisted quantum information processing: General protocols and nmr implementations. *arXiv preprint arXiv:1601.00234*, 2016.

[90] Abhishek Shukla, K. Rama Koteswara Rao, and T. S. Mahesh. Ancilla-assisted quantum state tomography in multiqubit registers. *Phys. Rev. A*, 87:062317, Jun 2013.

[91] Abhishek Shukla, K Rama Koteswara Rao, and TS Mahesh. Ancilla-assisted quantum state tomography in multiqubit registers. *Physical Review A*, 87(6):062317, 2013.

[92] Harpreet Singh, Kavita Dorai, et al. Experimentally freezing quantum discord in a dephasing environment using dynamical decoupling. *EPL (Europhysics Letters)*, 118:50001, 2017.

[93] Alexandre M Souza, Gonzalo A Álvarez, and Dieter Suter. Robust dynamical decoupling. *Phil. Trans. R. Soc. A*, 370(1976):4748–4769, 2012.

[94] Dieter Suter and Gonzalo A Álvarez. Colloquium: Protecting quantum information against environmental noise. *Reviews of Modern Physics*, 88(4):041001, 2016.

[95] Zdeněk Tošner, Thomas Vosegaard, Cindie Kehlet, Navin Khaneja, Steffen J Glaser, and Niels Chr Nielsen. Optimal control in nmr spectroscopy: Numerical implementation in simpson. *Journal of Magnetic Resonance*, 197(2):120–134, 2009.

[96] Tathagat Tulsi, Lov K. Grover, and Apoorva Patel. A new algorithm for fixed point quantum search. *Quantum Info. Comput.*, 6(6):483–494, September 2006.

[97] Lorenza Viola. Quantum control via encoded dynamical decoupling. *Phys. Rev. A*, 66(1):012307, 2002.

[98] Lorenza Viola, Emanuel Knill, and Seth Lloyd. Dynamical decoupling of open quantum systems. *Phys. Rev. Lett.*, 82(12):2417, 1999.

[99] Xiaoting Wang and SG Schirmer. Entanglement generation between distant atoms by lyapunov control. *Physical Review A*, 80(4):042305, 2009.

[100] Douglas Brent West et al. *Introduction to graph theory*, volume 2. Prentice hall Upper Saddle River, 2001.

[101] Jörg Wrachtrup and Fedor Jelezko. Processing quantum information in diamond. *Journal of Physics: Condensed Matter*, 18(21):S807, 2006.

[102] Yao-Ping Xie, Xiao-Jie Zhang, and Zhi-Pan Liu. Graphite to diamond: Origin for kinetics selectivity. *Journal of the American Chemical Society*, 139(7):2545–2548, 2017. PMID: 28166629.

[103] Theodore J Yoder, Guang Hao Low, and Isaac L Chuang. Fixed-point quantum search with an optimal number of queries. *Physical review letters*, 113(21):210501, 2014.

[104] Sixia Yu and CH Oh. Quantum pigeonhole effect, cheshire cat and contextuality. *arXiv preprint arXiv:1408.2477*, 2014.

[105] Alexander M Zaitsev. *Optical properties of diamond: a data handbook.* Springer Science & Business Media, 2013.

[106] Jingfu Zhang, Alexandre M. Souza, Frederico Dias Brandao, and Dieter Suter. Protected quantum computing: Interleaving gate operations with dynamical decoupling sequences. *Phys. Rev. Lett.*, 112:050502, Feb 2014.

[107] Jingfu Zhang and Dieter Suter. Experimental protection of two-qubit quantum gates against environmental noise by dynamical decoupling. *Phys. Rev. Lett.*, 115:110502, Sep 2015.

[108] Weiwei Zhou, SG Schirmer, Ming Zhang, and Hong-Yi Dai. Bang–bang control design for quantum state transfer based on hyperspherical coordinates and optimal time–energy control. *Journal of Physics A: Mathematical and Theoretical*, 44(10):105303, 2011.